Physics in Medicine & Biology

TOPICAL REVIEW

X-ray phase-contrast imaging: from pre-clinical applications towards clinics

To cite this article: Alberto Bravin *et al* 2013 *Phys. Med. Biol.* **58** R1

View the article online for updates and enhancements.

You may also like

- X-ray phase-contrast imaging: the quantum perspective
J M Slowik and R Santra
- Development of a synthetic phase contrast imaging diagnostic for turbulence studies at Wendelstein 7-X
S K Hansen, M Porkolab, J-P Bähner et al.
- A synthetic phase-contrast imaging diagnostic with spatial filtering for gyrokinetic simulations
A Iantchenko, S Coda, S Brunner et al.

JOIN US | ESTRO 2024
In-Booth Talks, Demos, & Lunch Symposium
Browse talk schedule >

This content was downloaded from IP address 18.119.125.7 on 05/05/2024 at 08:30

IOP PUBLISHING PHYSICS IN MEDICINE AND BIOLOGY

Phys. Med. Biol. **58** (2013) R1–R35 doi:10.1088/0031-9155/58/1/R1

TOPICAL REVIEW

X-ray phase-contrast imaging: from pre-clinical applications towards clinics

Alberto Bravin[1,4], **Paola Coan**[2] **and Pekka Suortti**[3]

[1] European Synchrotron Radiation Facility, 6 rue Horowitz, 38043 Grenoble Cedex, France
[2] Faculty of Medicine, Ludwig Maximilians University, Marchioninistrasse 15, D-81377 Grosshadern, Munich, Germany
[3] Department of Physics, University PL 64, FIN-00014 Helsinki University, Finland

E-mail: bravin@esrf.fr

Received 13 June 2012, in final form 20 August 2012
Published 10 December 2012
Online at stacks.iop.org/PMB/58/R1

Abstract

Phase-contrast x-ray imaging (PCI) is an innovative method that is sensitive to the refraction of the x-rays in matter. PCI is particularly adapted to visualize weakly absorbing details like those often encountered in biology and medicine. In past years, PCI has become one of the most used imaging methods in laboratory and preclinical studies: its unique characteristics allow high contrast 3D visualization of thick and complex samples even at high spatial resolution. Applications have covered a wide range of pathologies and organs, and are more and more often performed *in vivo*. Several techniques are now available to exploit and visualize the phase-contrast: propagation- and analyzer-based, crystal and grating interferometry and non-interferometric methods like the coded aperture. In this review, covering the last five years, we will give an overview of the main theoretical and experimental developments and of the important steps performed towards the clinical implementation of PCI.

(Some figures may appear in colour only in the online journal)

List of abbreviations

ABI:	analyzer-based imaging
AD:	Alzheimer's disease
CT:	computed tomography
DPC:	differential phase-contrast
DEI:	diffraction enhanced imaging
DM:	digital mammography
GI:	grating interferometry
MIR:	multiple-image radiography

[4] Author to whom any correspondence should be addressed.

 © 2013 Institute of Physics and Engineering in Medicine Printed in the UK & the USA

MRI:	magnetic resonance imaging
NFI:	near field imaging
OA:	osteoarthritis
PCI:	phase-contrast imaging
PBI:	propagation-based phase-contrast imaging
PPI:	phase propagation imaging
PSF:	point spread function
RA:	rheumatoid arthritis
SR:	synchrotron radiation
STDD:	sample to detector distance
(U)SAXS:	(ultra)small angle x-ray scattering

1. Introduction

In recent years, research and literature on x-ray phase-contrast imaging (PCI) methods for bio-medical applications has expanded almost exponentially. These developments have been reviewed at intervals every few years. General reviews (Suortti and Thomlinson 2003, Lewis 2004, Zhou and Brahme 2008) have been complemented by reviews of limited scope (Momose 2003a, 2005, Bravin 2003, Bech *et al* 2010b, Keyriläinen *et al* 2010, Appel *et al* 2011). These articles report extensive reference to earlier works. Conference proceedings of the medical applications of synchrotron radiation (SR) include many articles on PCI (Thomlinson *et al* 2008, Siu 2010), and a recent review of x-ray imaging technology also cites results in this field (Fouras *et al* 2009). The present review attempts to cover the main and most used PCI methods, and to give an overview of the preclinical and clinical bio-medical results obtained over the last five years. The physical foundations of PCI are presented with the aim of helping the reader in understanding and interpreting the information contained in the images. Special attention is paid to methods and results that may have a stronger impact for clinical applications, and, in this context, some details on the development of new x-ray radiation sources are also given. Finally, representative examples of the application of PCI to tissue and organ imaging are reported, guiding the reader towards the multiplicity of applications in biomedical imaging offered by the phase-contrast techniques.

2. Physical foundations of x-ray imaging

2.1. The refractive index

X-ray interaction with electrons of the target leads to collective, low-energy excitations of the system and to electronic excitations. These give rise to various forms of x-ray scattering: the scattered radiation carries information about electronic states and structures encountered during their travel to the detector. All scattering signals are potentially useful for medical imaging, and a short overview is given in the following.

X-ray PCI is based on the visualization of the wave front changes when radiation passes through an object. The transmitted wave is the resultant of the attenuated incident wave and the elastic forward scattering in the object. Elastic scattering and photoelectric absorption can be described fairly accurately in classical terms, which can be extended to quantum mechanical treatment (James 1962). Descriptively, the electromagnetic x-ray wave of amplitude $A_o(\mathbf{r}) = E_o(\mathbf{r}) \exp(-\mathrm{i}\omega t)$ makes the electron oscillate in the direction of the electric field E_o, and as an accelerated charge the electron radiates with frequency ω of the incident wave. The electrons are bound to atoms more or less strongly, except the outer electrons in metals,

and the classical equivalent of scattering from a bound electron is re-radiation from an electron in forced harmonic motion. The scattering amplitude is

$$f = -\omega^2 \big/ \left(\omega^2 - \omega_s^2 - \mathrm{i}\Gamma\omega\right) = -(f' + if''), \tag{1}$$

where ω_s is the natural frequency of the oscillating electron, and Γ a (radiation) damping factor. At high frequencies (i.e. $\omega \gg \omega_s$, which are used in most medical imaging), there is a phase shift of π in the scattered wave.

The resultant wave in the forward direction is obtained by calculating the forward scattering amplitude from Fresnel diffraction (i.e. near field diffraction) and adding that to the amplitude of the non-scattered wave. Using the construction of Fresnel zones for a thin sheet of the medium parallel to the incident wave-front, it is seen that the phase of the forward scattered wave lags $\pi/2$ behind the waves scattered by individual electrons, so that the total phase lag of the forward scattered wave is $3\pi/2$. Successive additions of these components $3\pi/2$ out of phase with the primary wave cause the resultant transmitted wave travel through the medium with phase-velocity larger than the velocity of light in free space, c, meaning that the refractive index of the medium is less than unity (James 1962)

$$n = 1 - r_e(N\lambda^2/2\pi)f = 1 - \delta - \mathrm{i}\beta \tag{2}$$

where N is the number of electrons per unit volume, and $\lambda = 2\pi/\mathrm{K}$ the x-ray wavelength. The amplitude of the resultant wave after thickness l of traversed medium is $E_o \exp(2\pi \mathrm{i} nl/\lambda) = A_o \exp[2\pi \mathrm{i}\delta l/\lambda] \exp[-2\pi\beta l/\lambda]$, where the first factor counts for the phase change, and the second for the decrease of amplitude.

The linear absorption coefficient (intensity loss per unit path length) is given by

$$\mu_o = 4\pi\beta/\lambda = 2\omega\beta/c = 2N\lambda r_e f'' \tag{3a}$$

and the coefficient of the change of phase ϕ by

$$\eta = 2\pi\delta/\lambda = \delta K = N\lambda r_e f'. \tag{3b}$$

For an atom, the contributions from different electrons are added up, and new notations are introduced. The real part of the atomic scattering factor is given by $f_o + \Delta f'$ (or by $f_o + f'$), and the imaginary part by $\Delta f''$ (or by f''). Here f_o depends on the scattering vector, $|\mathbf{k}| = (4\pi/\lambda)\sin(\theta/2)$, and in forward scattering $f_o = Z$, i.e. the number of electrons of the atom. The imaginary part is the sum of contributions from different electron shells, when ω is larger than the respective resonant frequency ω_s, and it turns out that each contribution to f'' falls approximately as $(\omega_s/\omega)^2$ with increasing frequency or energy of the incident x-ray photon.

The real and imaginary parts of the refractive index depend very differently on the energy of the incident x-ray photon. Sufficiently far above any resonance frequency and for light atoms, the coefficient of phase-shift is proportional to 1/E, where E is the photon energy E, while the absorption coefficient decreases approximately as $1/\mathrm{E}^3$. Also the numerical values of μ_o and η are very different, so that for light elements of human body tissue η is two-three orders of magnitude larger than μ_o at x-ray energies used in medical imaging. It is therefore obvious that variations in soft tissue density give rise to much stronger phase-contrast than to absorption-contrast. A 'complete' imaging experiment would yield the 3D distribution of both the real and imaginary parts of the scattering amplitude. The resolution of real space imaging is typically limited by the size of the detector pixel, but atomic or molecular structures become visible when the diffraction image of the object is Fourier transformed. Both real space imaging and reciprocal space imaging (Fourier imaging) are discussed in this review.

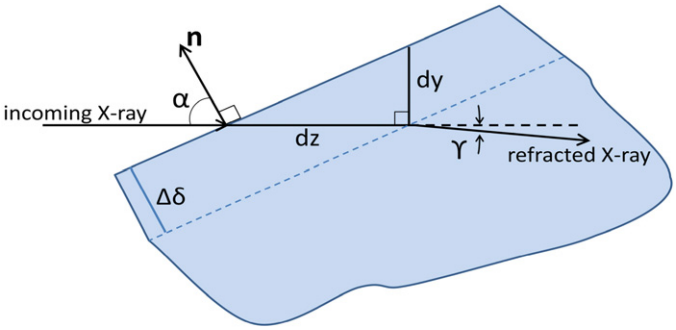

Figure 1. Representation of the refraction of an x-ray pencil beam within a sample. The refraction originates after an optical path dz, where the refractive index changes by $\Delta\delta > 0$ in the direction of the layer normal $\vec{n}$. The deviation of the beam is $\gamma = \Delta\delta \tan\alpha$. For simplicity, only the total refraction angle (equivalent to the sum of the refraction processes along dz) is represented.

2.2. *Scattering and refraction*

As discussed in section 2.1., the transmitted pencil beam is the resultant of the attenuated incident beam and the forward scattered beam. If the real part δ of the refractive index has a lateral gradient, the constant-phase front of the pencil beams is deviated, i.e. the x-ray wave is refracted. The refraction angle can be calculated using geometrical optics and Snell's law at an interface where the refractive index changes by $\Delta\delta$ (figure 1):

$$\gamma = \Delta\delta \tan\alpha, \tag{4a}$$

where α is the angle between the gradient (normal of the interface) and the incident ray, i.e. $\tan\alpha = \mathrm{dz}/\mathrm{dy}$, and from (3*b*)

$$\gamma = (\lambda/2\pi)\,(\mathrm{d}\phi/\mathrm{dy}). \tag{4b}$$

The expression diverges when the ray is tangent to the interface, and in practice this means sharp refraction contrast at the edge of the object. It has been verified by measurements on cylindrical objects that (4) holds quantitatively (Keyriläinen *et al* 2002).

Despite the origin of refraction being a lateral gradient in the amplitude of forward scattering, the term 'refraction' is reserved for cases where the deviation of the ray is observed at the detector or by an angular analyzer, arising from density variations in length scale of micrometers. Density variations of smaller scale blur refraction, so that the refracted beam may be considered being 'dressed' with a halo of small-angle x-ray scattering (SAXS). SAXS is confined so closely in the forward direction (< few mrad) that at least part of it is recorded together with the transmitted direct beam. Even if scattering is often considered a nuisance in medical imaging, this particular one, SAXS, carries essential information about the structure of the object. General properties of SAXS are described in the following using basic formulas of x-ray diffraction and Fourier transforms (Glatter and Kratky 1982, Feigin and Svergun 1987).

In units of the one-electron scattering amplitude, the amplitude from an object of electron density $\rho_o(\mathbf{r})$ and form factor $\tau(\mathbf{r})$ is

$$A(k) = \int \rho_o(\mathbf{r})\tau(\mathbf{r}) \exp(\mathrm{i}\mathbf{k}.\mathbf{r}) d^3\mathbf{r}. \tag{5}$$

Here $\mathbf{k}$ is the scattering vector, and $\tau(\mathbf{r}) = 1$ when $\mathbf{r}$ is inside the object and zero otherwise. By the convolution theorem, $A(\mathbf{k}) = A_o(\mathbf{k}) * T(\mathbf{k})$, where A_o and T are the Fourier transforms

of ρ_o and τ, respectively. The intensity of scattering is obtained by multiplying the amplitude by its complex conjugate and integrating over the volume $V(\mathbf{r})$ common to both the object and its 'ghost' at distance $\mathbf{r}$:

$$\mathrm{I}(\mathbf{k}) = \int P_o(\mathbf{r})\ \mathrm{V}(\mathbf{r})\ \exp(\,\mathrm{i}\mathbf{k}.\mathbf{r})d^3\mathbf{r} = F[P_o(\mathbf{r})] * |T(\mathbf{k})|^2\,. \tag{6}$$

Here $P_o(\mathbf{r})$ is the autocorrelation (Patterson) function of $\rho_o(\mathbf{r})$, and $|T(\mathbf{k})|^2$ is the Fourier transform of $V(\mathbf{r})$. Equation (6) actually contains all information available from an x-ray diffraction experiment. $F\ [P_o(\mathbf{r})]$ can be divided in parts that correspond to diffraction from the average structure and from the fluctuations of the structure. The first part is the central intensity maximum at $\mathbf{k} = 0$:

$$I(0) = |A(0)|^2 = [NF]^2, \tag{7}$$

where N is the number of scattering units of scattering amplitude F, which includes the wavelength-dependent dispersion factors $\Delta f'$ and $\Delta \mathrm{f}''$. The intensity distribution of the central maximum is given by $|T(\mathbf{k})|^2$, and this is the small-angle scattering term, which depends on the size and shape of the object, but not on its internal structure.

In the general case (6) cannot be inverted to yield $\tau(\mathbf{r})$, but certain properties can be deduced for isotropic distributions and objects of particular shapes. The width of $V\ (\mathbf{r})$ is inversely proportional to the width of $|T(\mathbf{k})|^2$, i.e. small particles give rise to wide SAXS, and scattering from large particles is confined to the regime of ultra-small-angle scattering (USAXS). In this regime, $|T(\mathbf{k})|^2$ can be expanded in power series and approximated by a Gaussian, so that at small values of $\mathbf{k.r}$ the so-called Guinier approximation is obtained (Guinier 1939):

$$I(k) = I(0)\ \exp[-kR_g)^2/3], \tag{8}$$

where R_g is the radius of gyration of the electron density distribution of the object. The Guinier approximation has a rather narrow range of validity, but nevertheless, the Gaussian approximation has been frequently used to describe USAXS.

The above formulation of SAXS is strictly valid only for an isolated object. Even in the case of independent objects, the SAXS intensity is convolved by the size and shape distribution of the objects. In a real object, like in a tissue sample, the scattering entities are closely packed, so that the scattering amplitude should be calculated for an extended volume. However, at sufficiently large values of $\mathbf{k}$ even small variations in distance $\mathbf{r}$ to neighboring objects lead to destructive interference, so that the independent particle approximation is valid. At the far slope the SAXS intensity distribution follows a power law (Porod 1951):

$$I(k) = 2\pi\rho_o^2\ S\ k^{-q}. \tag{9}$$

Here S is the surface area of the particles of the object in unit mass. Before reaching the final slope, where $q = 4$, different values of the slope exponent are observed, depending on the shape of the object. The exponent q is 4 for three-dimensional objects with continuous outer surface, 2 for two-dimensional disks, 1 for rods, 2 or 5/3 for coils, and between 1 and 4 for different mass and surface fractals (Schmidt 1991). The power law exponent and specific surface are important parameters, which characterize the object, and can be utilized for imaging of molecular and supra-molecular structures of tissues.

3. Phase-contrast imaging methods

The goal of PCI is to determine 2D (radiography) or 3D (tomography) distributions of the scattering properties of an object (related to the electron density, see equations (2) and (3)) by recording attenuation and phase changes of the transmitted x-ray beam.

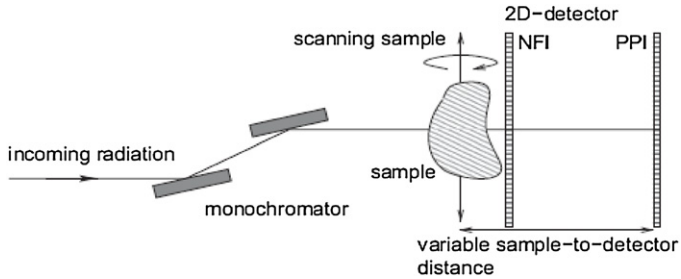

Figure 2. The experimental set-up of PBI. A monochromatic, transversally coherent x-ray fan beam traverses the sample, and is recorded by a 2D detector at different distances. PPI, phase propagation x-ray imaging (another name of PBI); NFI, near field imaging. Reprinted from Keyriläinen *et al* 2010 *Acta Radiol.* **51** 866–84. Copyright 2010, Royal Society of Medicine Press, UK.

Various techniques have been developed to exploit the phase-contrast in the x-ray regime. They can be classified into five main categories: the propagation-based imaging (PBI) methods (Snigirev *et al* 1995), the analyzer-based imaging (ABI) methods (Förster *et al* 1980, Davis *et al* 1995), the interferometric methods based on the use of crystals (Bonse and Hart 1965, Momose *et al* 1996), the grating interferometric (GI) (Weitkamp *et al* 2005) and the grating non-interferometric methods (Olivo and Speller 2007).

These methods differ not only for their experimental set-up and requirements in terms of the x-ray beam spatial and temporal coherence, but also for the nature and amplitude of the provided image signal, and for the amount of radiation dose that is delivered to the sample. These PCI modalities have been extensively investigated in preclinical and clinical trials to access their potential for biomedical imaging. Despite the large number of publications in the field of phase-contrast, very few attempts have been made to compare these different methods (Pagot *et al* 2005, Diemoz *et al* 2012a, 2012b) and a complete qualitative and quantitative comparison is still missing in the literature.

For each of these techniques, the final image contrast depends on several factors, including the spatial resolution of the x-ray detector, the specific image formation mechanism, x-ray energy and the beam divergence. An extensive discussion of these individual contributions for PBI, ABI and GI is given in (Diemoz *et al* 2012a).

3.1. Propagation-based phase-contrast imaging

Experimentally the simplest way to visualize the phase-contrast is the propagation-based phase-contrast imaging (PBI) method (also indicated as 'phase propagation imaging'), which is analogous to in-line holography. No reference wave is required, when a coherent wave-front traverses the sample and the distorted wave-front propagates sufficiently far, so that the small differences in phase propagation cause interference, and variations of intensity are observed in the image plane (figure 2). Under quite general conditions, the lateral Laplacian of phase $d^2\phi/\mathrm{d}x^2 + d^2\phi/\mathrm{d}y^2$ (with the x-ray beam propagating along the z direction) is proportional to the longitudinal gradient of intensity (Teague 1983). This differential transport-of-intensity equation (TIE) can be solved to yield ϕ when the incident intensity is known and the transmitted intensity is recorded at a suitable distance, or at two or more distances in the linear regime. Phase retrieval from TIE is valid under certain conditions, as discussed below. Since the total phase change determined by the object is proportional to the projected electron density (3*b*), phase CT imaging can be applied (section 4.1). Phase retrieval may not be necessary to obtain useful results, because the edge-enhancement property of PBI visualizes the object

structure without further data processing. In a sample, the phase changes are mainly occurring at the boundaries between two details or at the borders of the object itself, and therefore the contrast arising from the lateral Laplacian of phase emphasizes the internal and external contours. Examples of the edge enhancement are illustrated in section 8. In actual imaging the phase-contrast signal is convolved with the detector modulation transfer function and with the demagnified source size. Phase-contrast can be visualized if the transverse coherence is sufficient, i.e. the lateral extent of the well-defined wave-front, $L_{\mathrm{coh}} = \lambda R/s$, is larger than the detail a to be imaged (here R is the distance to the source of size s). The requirements of coherence have been discussed in detail by Wu and Liu (2007). Already early experiments showed that small objects can be imaged with high spatial and contrast resolution using polychromatic radiation from a micro-focus x-ray tube (Wilkins *et al* 1996), which is important for potential clinical applications (Kincaid *et al* 2008).

It has been demonstrated that the PBI signal for a given spatial frequency f is maximum when it is recorded at a distance $\mathrm{d} \sim 1/2\lambda f^2$. In order to retrieve the 3D electron density map, which is useful in several applications, specific reconstruction algorithms have to be applied to the acquired CT images. Methods have been summarized by Nugent (2007), and the practical aspects have been discussed in detail recently (Gureyev *et al* 2009, and references therein). In most cases of imaging of biological samples, the Fresnel number $N_F = a^2/\lambda d \gg 1$, and the so-called TIE holds. If a single imaging distance is used, additional assumptions are needed to untangle the contributions of absorption and phase. In soft tissue imaging at energies higher than 30 keV, Compton scattering dominates in attenuation, so that both δ and β are proportional to the local density of the object, and their ratio is constant throughout the 'monomorphous' object (Paganin *et al* 2002, Wu and Liu 2005, Chen *et al* 2011b). The phase retrieval methods and their approximations have been studied in detail, listing similarities and differences between seven commonly used algorithms (Burvall *et al* 2011).

There is continuing interest and research in the development of the PBI method. Recent literature includes basic work on foundations and limiting assumptions, going beyond linearity, small phase gradients and the assumption of large Fresnel number in phase retrieval (Hofmann *et al* 2011, Moosmann *et al* 2010, 2011, Eastwood *et al* 2011, Wu and Yan 2009, De Caro *et al* 2008). Several experimental and computational developments have been put forward (Guo *et al* 2011, Luu *et al* 2011, De Caro *et al* 2010, 2011, Ren *et al* 2011, Anastasio *et al* 2009, 2010, Kashyap *et al* 2010, Gong *et al* 2010, Irvine *et al* 2010, Beltran *et al* 2010, Olivo and Speller 2009, Meng *et al* 2009, Chou and Anastasio 2009, 2010). Detailed descriptions of the factors affecting image contrast, signal-to-noise ratio and spatial resolution have been given by Gureyev *et al* (2008).

3.2. Analyzer-based imaging

Analyzer-based imaging (ABI) is the generic term for methods known by various terms and acronyms: 'Schlieren' method, refraction-contrast radiography/introscopy, phase-dispersion imaging, diffraction imaging, diffraction-enhanced x-ray imaging (DEI), multiple image radiography (MIR) (the last two ones often used to indicate both the technique and a specific image reconstruction algorithm); for references see Bravin (2003) and Keyriläinen *et al* (2010). All ABI methods utilize quasi parallel and monochromatic x-ray beams, and perfect crystal analyzers. The analyzer acts as a very narrow angular slit, reflecting only the rays that make the correct angle (Bragg angle) with the atomic (Bragg) planes of the crystal. A single image taken along the reflectivity curve of the analyzer crystal can be sufficient in several cases to make a diagnosis, despite it contains mixed absorption and refraction signals. By recording

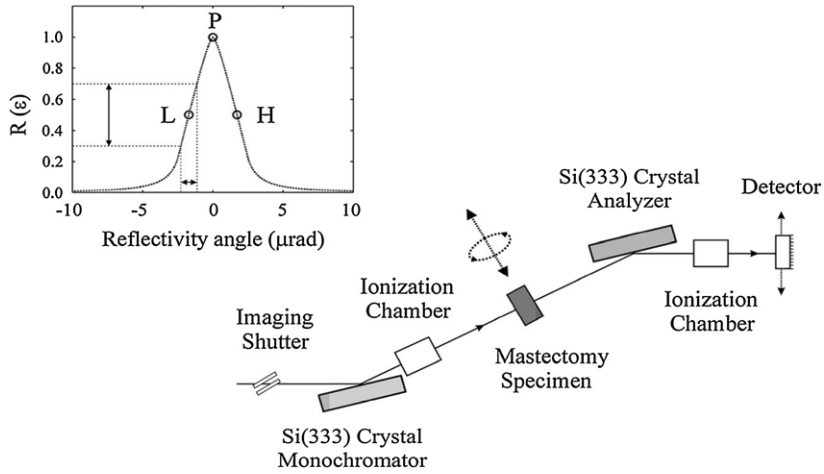

Figure 3. Schematic diagram of an ABI set-up. The diffraction optics includes a high-spatial-resolution monochromator and analyzer crystals. The graph shows the reflectivity curve, R(ε), of silicon 333 (Si 333) reflection at 30 keV and the principle of the analyzer-based x-ray imaging method. The reflectivity curve demonstrates the conversion between the angular x-ray deviations (horizontal axis) and the intensity changes (vertical axis), as shown by the arrows. P, L, and H indicate the peak, low-angle, and high-angle positions on the reflectivity curve, respectively. Reproduced, with permission, from Keyriläinen *et al* 2008 *Radiology* **249** 321–7.

images at different angles, the non-deviated, refracted and scattered rays can be separated. In a typical case the full width at half maximum (FWHM) of the reflectivity curve is a few microradians, and its shape is approximately triangular with linear slopes.

A typical ABI set-up is shown in figure 3, where the analyzer is tuned to reflect at the angle that corresponds to the peak of the intrinsic (without an object) reflectivity curve (top), or at the mid-slope on either side of the reflectivity curve (low or high). At top, scattering and refracted rays are rejected, leading to the so called apparent absorption (or extinction) contrast. At the low and high positions, the changes in propagation direction are converted to intensity changes called refraction-contrast (Chapman *et al* 1997).

Actually, the ABI set-up is a Bonse–Hart camera in its simplest form (Bonse and Hart 1966), and can be used for mapping (or rejecting) the small- and ultra-small-angle scattering ((U)SAXS) created by the sample. Several algorithms have been put forward to separate the attenuation, refraction and scattering signals and some of the most cited in the literature have been reviewed and compared quantitatively (Diemoz *et al* 2010a, 2010b). The common feature of several algorithms is the use of Taylor expansions at the working points of the rocking curve (RC). In the original DEI algorithm (Chapman *et al* 1997) only two working points at the opposite linear slopes of the intrinsic RC are used, and the difference and sum of the intensity values yield the refraction angle and apparent absorption, respectively. The possible broadening of RC due to USAXS is ignored, and this requires introduction of higher order terms in the Taylor expansion, and at least three working points (Rigon *et al* 2007, Chou *et al* 2007). A Gaussian function has been used to describe USAXS and SAXS, either explicitly (Oltulu *et al* 2003, Wernick *et al* 2003) or implicitly (Pagot *et al* 2003), (Nesterets *et al* 2006b), which allows for parametric presentation of the difference of the RC with respect to the intrinsic RC by the zeroth moment (attenuation), first moment (refraction) and second moment (scattering). The term 'multiple-image radiography' (MIR) has been

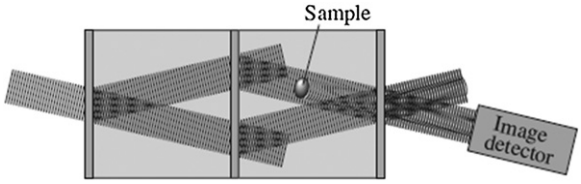

Figure 4. Scheme of the first crystal x-ray interferometer reported by Bonse and Hart in 1965. The entire body of the interferometer was monolithically cut out from a silicon crystal. Three parallel lamellae are formed with a constant spacing. The lamellae function as beam splitters when an x-ray is incident at the Bragg diffraction condition on a lattice plane perpendicular to the surface of the lamellae. The amplitude of an x-ray is coherently divided into diffracted and forward-diffracted beams outgoing from the opposite side of the lamella. X-rays thus divided by the first lamella are divided again by the second lamella in the same manner. Two beams overlapping at the third lamella are also divided and interference is observed in the beams outgoing from the third lamella. Reprinted from Momose *et al* 2005 *Japan J. Appl. Phys.* **44** 6355–67. Copyright 2005, The Japan Society of Applied Physics.

coined to this approach, and application to CT imaging has been presented (Khelashvili *et al* 2006). However, the ABI set-up is a 'long-slit' instrument, where scattering is integrated in the direction perpendicular to the diffraction plane, sometimes giving rise to extended tails of the RC. A detailed discussion and references to earlier work is given by Suhonen *et al* (2007). Voigtian or pseudo-Voigtian functions are used to describe the observed RCs with different samples. Subsequent studies have demonstrated that even better description of the RC is obtained by the use of Pearson VII function (Kitchen *et al* 2007, Fernandez *et al* 2008), particularly when a Laue-type (transmission) analyzer crystal is used (Kitchen *et al* 2010, 2011).

When ABI is used for tissue or organ imaging often a single image is sufficient to allow for a diagnosis, as already mentioned. Nevertheless, when phase retrieval or separation of refraction from absorption-contrast is required, more images are necessary. Algorithms based on adequate curve fitting by Pearson VII or Voigt functions require images at five positions along the RC, while two or three images are sufficient in Taylor expansion- and Gaussian-based algorithms.

3.3. Crystal interferometry

Crystal interferometry combined with CT imaging is a direct experimental method for mapping the scattering properties of the object from measurements of the phase changes occurred within the object. The interferometer was introduced by Bonse and Hart (1965), and an instrument suitable for bio-medical imaging was constructed in 90s (Momose 1995). Recent developments and applications have been reviewed by Momose (2003a, 2005). In its simplest form the interferometer consists of three parallel silicon crystal wafers, which stick out from a monolith perfect crystal ingot (figure 4). The incident x-ray beam is diffracted and split in two identical monochromatic wave-fronts in the first wafer (S), and these beams are split again in the second wafer (M). The inner beams join in the third wafer (A), and the interference pattern is recorded by an area detector. A wedge-shaped phase shifter in one of the beams gives straight interference fringes with regular intervals (carrier fringes), and when the object is placed in the other beam the fringes bend. The displacement of the carrier fringes corresponds to the phase shift caused by the object. The phase map in a single projection can be constructed faster using a Fourier method (Takeda *et al* 1982).

The interferometric method works best for small and smooth phase gradients. Its intrinsic constraints arising from small field of view (a few centimeters), and from the extreme requirements of stability and alignment of the interferometer have contributed to limit the dissemination of the technique.

3.4. Grating interferometry

Grating interferometry (GI) (now also indicated as 'differential phase-contrast imaging, DPC') with x-rays is based on an optical phenomenon discovered in early 19th century (Talbot 1836), and explained as Fresnel diffraction in a periodic grating (Rayleigh 1881). The image of the grating is repeated at regular distances behind the grating,

$$d_T = 2p^2/\lambda, \tag{10}$$

where p is the period of the grating. At fractional distances the same patterns appear shifted and/or with fractional period.

In x-ray applications a phase grating is used, where the grooves produce a periodic variation in the phase of the wave-front behind the grating. From (3b), the phase difference is $\eta h = \delta \mathrm{K} h$, where h is the depth of the groove. Interference after a pure phase grating reproduces the phase pattern at multiples of the half Talbot distance, but intensity modulation is observed at fractional distances. In particular, behind a π phase variation grating, where the groove width is $p/2$, a square-wave like intensity pattern of period $p/2$ is observed at fractional Talbot distances:

$$D = mp^2/8\lambda, \tag{11}$$

where m is an integer. In the standard configuration, an absorption grating of period $p_2 = p/2$ is placed in front of the detector, and the pattern is recorded by scanning the grating across the detector (phase-stepping). In first order, the intensity varies sinusoidally:

$$I(X_g) = a_o + a_1 \cos\{2\pi x_g/p_2 + \phi_1\}, \tag{12}$$

where x_g is the displacement of the grating, and ϕ_1 the phase shift. The average intensity, including background, is a_o. The phase shift is zero when there is no object in the x-ray beam. When an object is placed in the beam, in front or behind the phase grating, the wave-front is deviated by refraction, and the intensity pattern is shifted (figure 5). Evidently, transverse coherence over a phase grating period is required. In phase-stepping, a_o, ϕ_1 and a_1 are recorded at each detector pixel, and when compared with those without the object, three images are obtained: absorption, differential phase shift and dark field. In other terms, the 'differential phase shift image' maps the refraction properties of the sample while the 'dark field image' maps the scattering properties.

Since its introduction about ten years ago (David *et al* 2002, Momose *et al* 2003b) and subsequent developments, x-ray GI has become a widely used PCI method (Takeda *et al* 2008, McDonald *et al* 2009, Weitkamp *et al* 2008). The Talbot distance is inversely proportional to the x-ray wavelength, so that there is certain depth-of-field in the intensity pattern, which allows use of polychromatic radiation from an x-ray tube. There are already several carefully studied experimental set-ups, which might open clinical perspectives for GI (Pfeiffer *et al* 2006, Herzen *et al* 2009, Stutman *et al* 2011, Donath *et al* 2010, Zambelli *et al* 2010). The development of the technique has been performed mainly using SR sources. Microfocus x-ray tubes provide sufficient transverse coherence of the wave-front, but the intensity is low. High-power rotating anode x-ray tubes can be used when the source is split to an array of line sources by placing an additional absorption grating close to the tube focus. This set-up is called Talbot–Lau interferometer (Pfeiffer *et al* 2006, Bech *et al* 2009b). Alternative

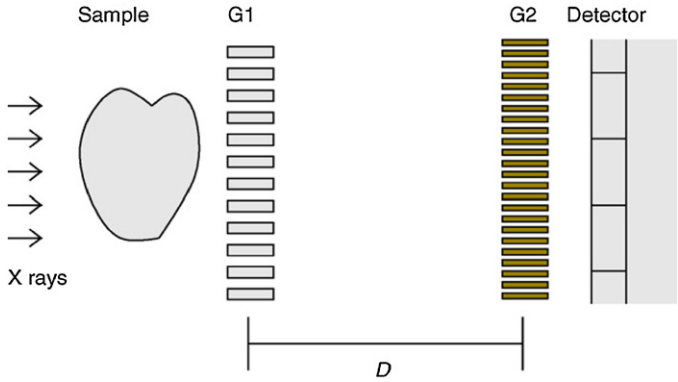

Figure 5. Schematic set-up of GI. A pattern of x-ray interference fringes is formed downstream a linear diffraction grating G1 (beam splitter); its local distortions from its ideal regular shape contain information on the sample structure. Since the fringes are too closely spaced to be resolved by the pixel detector used to record images, an additional absorption grid (G2, analyzer grating) in front of the detector is needed to transform fringe-position information into intensity values on the detector pixels. Reprinted from Weitkamp *et al* 2008 *Eur. J. Radiol.* **68** S13–7. Copyright 2008 with permission from Elsevier.

experimental set-ups have been put forward, and the effects of partial transverse coherence and polychromatic source have been analyzed (Nesterets and Wilkins 2008, Wang *et al* 2010a, 2010b, Ge *et al* 2011, Du *et al* 2011), as well as signal and noise propagation (Revol *et al* 2010, Tang *et al* 2011a, Weber *et al* 2011, Chen *et al* 2011a, Raupach and Flohr 2011, Modregger *et al* 2011, Thuering *et al* 2011). A detailed analysis has been published on the geometrical factors affecting the performance of the Talbot–Lau interferometer (Wen *et al* 2011).

The phase-stepping method requires image recording at minimum of three positions x_g, and, for that purpose, large precision and stability are needed. When $x_g = p_2/4$, the interferometer is tuned to the slope of the intensity curve, and the differential phase ϕ_1 is linear with small intensity changes. Phase stepping is avoided, and the exposure time and radiation dose are reduced, but only the absorption or refraction image is obtained (Wen *et al* 2008, Zhu *et al* 2010). Slight rotation of the absorption grating and Fourier decomposition of the Moiré pattern (see below) has been used to retrieve CT images of absorption, refraction and scattering without phase-stepping (Bevins *et al* 2012).

The phase and scanning gratings are periodic in one direction, so that the images arise from beam deviation in that direction only. Two-dimensional phase-contrast images have been recently obtained by separate perpendicular scans at the cost of doubling exposure and radiation dose (Kottler *et al* 2007). A 2D grating interferometer has been constructed and tested (Zanette *et al* 2011). However, it has been demonstrated that 2D refraction CT images are obtained when the phase and analyzer gratings are tilted with respect to the rotation axis of the object (Rutishauser *et al* 2011). A two-dimensional chess-board grating (with phase modulation of π) has been used to create a Talbot self-image of half-period (Itoh *et al* 2011, Sato *et al* 2011). In this latter case, the absorption grating is rotated slightly to form a Moiré fringe pattern at the detector position. Fourier transform of the pattern separates absorption and differential phase components, and by inverse transform, absorption and phase images are obtained from a single exposure. 2D phase grating has been used also together with a high-resolution detector without the absorption grating (Rizzi *et al* 2011). Advantages of 2D versus 1D GI have been demonstrated also by numerical simulations (Jiang *et al* 2008).

3.5. Other grating non-interferometric methods

There are several methods where the incident beam is periodically modulated by an absorption grating, and the distortion of the regular pattern introduced by the object is recorded and analyzed. The Talbot interference is not exploited, and the detector distance from the grating is chosen to provide sufficient angular resolution. Some of the contrast resolution of standard GI is lost, and background is higher, but the methods are simple and easily implemented.

In a single exposure method introduced for fast *in vivo* animal imaging the beam is split in an array of laminar beams, which is recorded as the reference image. The local transverse phase shift due to refraction in the object is obtained directly from the image (Morgan *et al* 2011b). In a similar set-up the image at the detector is Fourier-transformed to a spatial frequency spectrum, which is the sum of a series of harmonic spectra. These can be separated to yield absorption, refraction and even scattering images (Bennett *et al* 2010, Liu *et al* 2011). The methods have been extended to 2D absorption gratings, and applied for *in vivo* animal imaging (Wen *et al* 2010, Morgan *et al* 2011a).

In the coded-aperture method the detector is divided by a mask into a pattern of sensitive and insensitive regions between adjacent pixels, and a pre-sample mask creates the same pattern of beams that impinges on the boundaries of sensitive and insensitive regions. The original idea dates back to Olivo *et al* (2001) and was further developed in the recent years (Olivo and Speller 2007, Munro *et al* 2010a, 2010b, Olivo *et al* 2011). The beams are deviated by refraction in the sample, resulting in intensity variation at the detector. The set-up is very simple, and polychromatic radiation from an x-ray tube can be used (Ignatyev *et al* 2011). The implementation of the technique at x-ray energies close to 100 keV has been already demonstrated, opening promising perspectives in view of potential clinical applications (Olivo *et al* 2012). In a similar set-up, used for imaging small tissue samples, the beams fall on the borders of adjacent detector pixels, and shifts due to refraction are recorded by the imbalance of intensity (Krejci *et al* 2010).

3.6. Scattering and dark-field imaging

It has been already mentioned in section 2 that scattering from the sample provides essential information about the micron and sub-micron structures of the object, i.e. on the cellular and supra-molecular level. SAXS measurements that could be used for solution or reconstruction of these fine structures require dedicated instruments, such as pinhole cameras and high-resolution area detectors. Many tissues are hierarchical structures, and these give rise to distinct features in the diffraction patterns. The structure may be modeled and the diffraction pattern computed as a function of a few parameters, which are determined from comparison with the experimental SAXS intensity (Suhonen *et al* 2005). As an example, a structure of particular importance is that of fibrous collagen. Triple helices of amino acid chains pack together to form fibrils, which are about 50 nm in diameter, and have axial periodicity of about 65 nm. The fibrils aggregate in a quasi-hexagonal manner to form fibers, but the fibril diameter and packing distance may vary substantially. This model has been used to extract the structural parameters of the actual collagen I in human breast tissues, and it is found that cancer invasion causes changes in the tissue structure, which become visible in the SAXS pattern (Fernandez *et al* 2008, Sidhu *et al* 2009). It is worth mentioning that also wide-angle elastic scattering (WAXS) has been used for breast tissue characterization, and a method for cancer diagnosis on the basis of the scattering pattern from biopsies has been put forward (Ryan and Farquharson 2007).

PCI methods that have high angular resolution provide a scattering image of the object. If the RC in ABI is decomposed adequately, angular distribution of scattering projected on the plane of diffraction is obtained (Suhonen *et al* 2007, Kitchen *et al* 2011). In GI the signal of total scattering is obtained from the minimum intensity in phase-stepping recording (Modregger *et al* 2012, Bech *et al* 2010a, Wang *et al* 2009, Pfeiffer *et al* 2008). Most algorithms that are used to separate the effects of absorption, refraction and scattering assume a Gaussian distribution of small-angle scattering, although this assumption ignores the long tails of SAXS intensity.

Extraction of the scattering signal typically requires intensity recording at several steps of the analyzer grating in GI or at several rocking angles of the analyzer crystal in ABI. Simultaneous segmentation of the beam transmitted by the object to the strictly forward beam and the deviated beam by a Laue-type analyzer crystal has been demonstrated (Ando *et al* 2008). However, the effects of refraction and scattering are not separated in this method.

4. Image analysis

4.1. Foundation of CT Phase-contrast imaging

At distance z along the beam path within the sample, the x-ray attenuation is described by $\mu(x, y, z)$, refraction by the lateral phase gradient grad$\phi(x, y, z)$, and scattering by the scattering (diffusion) coefficient $\sigma(x, y, z)$ (Bech *et al* 2010a, Rigon *et al* 2008, Khelashvili *et al* 2006). CT imaging is based on the assumption that when the cumulative effects of these factors on a pencil beam are recorded and separated behind the sample, the values of μ, gradϕ and σ can be reconstructed from a sufficient number of projections. This implies that the pencil beam travels in the object within the infinitesimal channel defined the detector pixel. Some dimensions may be useful: if the object thickness is 100 mm, the sample-to-detector distance (STDD) is 1000 mm, and the detector pixel size 10 μm, the channel width is 10 μrad. In a typical case of ABI the RC width as FWHM is 1.5 μrad (Si(333) analyzer with 50 keV radiation). The scalar components of the refraction angle in the plane of diffraction (y, z) add up, and at the exit the angular deviation is the line integral of the refraction angles. When the y-direction is the rotation axis, the phase gradient $\mathrm{d}\phi(x, y, z)/dy$ is the same at all rotation angles, but if the rotation is about the x-axis then a different CT algorithm is required (Maksimenko *et al* 2005). The situation in SAXS is more complex. Multiple refraction blurs the pencil beam, and in dense distributions of similar objects, such as alveoli in lung, this results in variable focusing and speckle in the image plane. Monte Carlo simulations for such a case indicate that typical blurring is Gaussian of about 10 μrad FWHM (Kitchen *et al* 2004). The effects of multiple refraction are not separable from USAXS or SAXS, although SAXS originates from diffraction in much smaller structures. From Guinier's approximation, the FWHM of the SAXS pattern is $\Delta\theta = 2.9/(KR_g)$, where $K = 2\pi/\lambda$ is the wave-vector and R_g radius of gyration of the scattering particle. For instance, with 50 keV radiation $\Delta\theta = 0.3$ mrad for a sphere of 100 nm. The SAXS pattern varies in width and intensity within the object, and the original pencil beam may spread over many pixels at the detector.

The intensity distribution at distance z of the attenuated and refracted x-ray is convolved by the scattering probability function between z and $z+dz$, i.e. by a δ-function (no scattering) plus the function $|T_z(\mathbf{k})|^2$ (equation 6). The Fourier transform of $|T_z|^2$ is $V_z(\mathbf{r})$, the integral of which is proportional to the scattering coefficient $\sigma(x, y, z)$ per unit path length. Using the convolution theorem, the successive convolutions of the intensity distribution is written as the inverse Fourier transform of the successive multiplications of the corresponding $V_z(x, y)$. Fourier transform of the intensity distribution of scattering behind the object gives this product.

The parameter to be extracted from the reconstructed CT image is $V(\mathbf{r})$, i.e. the Fourier transform of the local scattering distribution $|T(\mathbf{k})|^2$. In general, this is a multi-parameter function, so that for an algorithm a simple functional form is used, and in all applications the Gaussian function has been adopted. The advantage is that the Gaussian form is retained in successive convolutions and multiplications, and in Fourier transform. The transmitted intensity is reduced by SAXS exponentially, and the exponent is a line integral of the local scattering cross section and number density of particles. Standard CT reconstruction methods are used yielding a map of characteristic sizes of the scattering particles (Chen *et al* 2010). Extraction of different signals and combination with reconstruction algorithms for various experimental set-ups have been discussed in many recent studies (Huang *et al* 2007, Cong *et al* 2012, Lauzier *et al* 2012, Li *et al* 2012, Chou and Huang 2011, Köhler *et al* 2011, Chen and Qi 2008).

In summary, when the effects of absorption, integrated phase change, and scattering are separated in a projection image, CT imaging and reconstruction of the respective object parameters are possible. Absorption and phase distributions are well defined, but the inversion of the object structure and composition from the scattering pattern is model-dependent.

4.2. Phase retrieval

The performances and limitations of different PCI methods may be compared at different levels: the visibility and separability of various signals, the adequacy of the algorithms used for the retrieval of the object properties from these signals, and the potential application of the method in clinics.

All practical phase retrieval algorithms include more or less stringent validity conditions or assumptions in order to keep the algorithms manageable. The TIE is used in PBI, and the geometrical optics approximation (GOA) in ABI. These imply either slow variation of the x-ray phase in the length scale of the first Fresnel zone width (in PBI), or of the extinction length of the analyzer crystal reflection (in ABI). Evidently, these conditions become critical in the proximity of the contours of the object, where the lateral gradient of the phase is large, or when the objects presents fine features. Failures of TIE have been illustrated, and alternative algorithms have been put forward, such as the mixed TIE and contrast-transfer-function (CTF) (Langer *et al* 2008, Gureyev *et al* 2004), and the attenuation-partition (AP)-based algorithm (Yan *et al* 2011). The small-scale variations, which are not resolvable by the imaging system, give rise to multiple refraction and small-angle scattering, and the loss of intensity in the strict forward direction is called 'decoherence effect' in PBI and 'extinction effect' in ABI. A wave-optical treatment has been given by Nesterets (2008) and applied in PBI and ABI, and an extension to cone-beams and GI has been given by Lynch *et al* (2011). When the object is divided to resolvable and unresolvable structures, then modified TIE and GOA are obtained. The propagation-contrast image of the resolvable structures is attenuated by incoherent scattering to diffuse background, and in ABI the extinction loss is found as increased intensity in the tails of the RC. This scattering contribution from the unresolvable structures is a useful source of information about the object on sub-micron level.

When the distance from the object to the detector is sufficiently large, ABI and PBI signals are mixed, and a combined imaging method has been suggested (Coan *et al* 2005). A general expression for the intensity at the image plane has been derived, and explicit forms under the assumptions of weak-object and validity of GOA have been also given (Nesterets *et al* 2006a, 2006b). Methods for the numerical wave-optical simulations of ABI including the free-space propagation to the detector have been given by Bravin *et al* (2007).

A very recent method has been proposed by Munro *et al* (2012) and applied to their grating non-interferometric method. They presented a truly incoherent phase retrieval method, which removes the spatial coherence constraints and employs a conventional source without aperturing, collimation or filtering. This technique can become important in applications where exposure time and radiation dose are critical.

5. Comparison of the different PCI techniques

A detailed and balanced comparison between the PCI methods in terms of detail visibility and clinical relevance does not exist yet. From published works, it is not possible to extrapolate data for an *a-posteriori* evaluation because of the large variety of experimental conditions applicable to the different techniques (subject also discussed in detail later on). Each PCI method may be applied with several experimental and set-up parameters. In principle, these parameters should be optimized in order to maximize the sensitivity of the technique depending on the characteristics of both the sample to be investigated and the source/x-ray beam (e.g. source size and divergence, spatial and longitudinal coherence, divergence, energy, etc). In practice, the actual experimental configurations are determined by mechanical and/or laboratory limitations (for instance, possible STDDs, available detector spatial resolution, translation/rotation motor resolution, optics stability, etc).

For all these reasons, there are only very few meritorious attempts to theoretically and/or experimentally compare the techniques in terms of their sensitivity and performance. Detailed experimental comparisons need *ad-hoc* experiments, performed with same physical parameters: source characteristics, energy, divergence, etc. Only very few laboratories in the world have the possibility of installing and using the different PCI set-ups on the same x-ray source. Similar considerations apply to dose and acquisition time aspects because of the large variety of spatial resolutions, detector efficiencies, x-ray energies and sample characteristics used by the different methods and works. It has been shown that both ABI and PBI can produce images at doses that comply with recommendations in clinical practice (examples are included in section 8). To our best knowledge, a few dose estimates are given for GI: Stampanoni *et al* (2011), Richter *et al* (2009), Tapfer *et al* (2012). Values reported there indicate that further development is necessary for making the technique compatible with *in vivo* applications.

To our knowledge, the only published studies comparing two or more PCI techniques are Diemoz *et al* (2012a, 2012b), Yoneyama *et al* (2008) and Pagot *et al* (2005). In this last article, the imaging parameters such as the energy, the angular position of the analyzer crystal in ABI or the STDD in the PBI case were varied in order to optimize the image quality in terms of contrast, visibility and figure of merit (signal-to-noise ratio divided by the square root of dose). The information given by the two techniques was reproduced by theoretical simulations and experimentally compared for different kinds of samples (phantoms and biological tissues). These results were confirmed and extended by Diemoz *et al* (2012a, 2012b). In these studies, the PBI, ABI and GI methods were theoretically and analytically compared for the first time by using the same phantoms, x-ray source and detector. A comprehensive analysis in terms of area- and edge-signal-to-noise (SNR) and figure-of-merit (FoM, necessary for comparing images obtained with different doses) was carried out. Theoretical expressions and analytical estimations for these quantities can be useful in the setting up of experiments, allowing choosing the best technique and experimental conditions according to the properties of the object to be imaged and the experimental requirements (such as dose constraints, the needed spatial resolution, etc).

Among other results demonstrated in these two works, it was shown that the FoM in the PBI technique differ considerably from those obtainable using either the GI or the ABI. PBI is expected to have maximum sensitivity for higher object spatial frequencies (i.e. slowly varying electron densities) than ABI and GI do. PBI is more affected by the system finite spatial resolution than the other techniques: it provides higher FoM when the width of the detector point spread function (PSF) is very small. The achievable spatial resolution in ABI (without using magnifying set-ups) is limited to few microns by the penetration depth of the x-rays in the analyzer and hence depends on the chosen energy and reflection extinction length in the crystal, determined by the dynamical diffraction effects. However, good spatial resolution in PBI requires high spatial coherence of the beam, which is not as necessary for the ABI technique. Important analogies exist between the signal in the ABI and GI techniques: in both cases the edge FoM is to first approximation proportional to the refraction angle. The FoMs are also proportional to the first derivative of the RC (in ABI) and of the phase stepping curve (in GI). Therefore, the sensitivity of the techniques is maximized around the slopes of these functions, where their first derivative is maximum, and reaches the lowest values at the top and bottom positions, where the derivative is equal to zero. Diemoz *et al* (2012a, 2012b) have also studied the dependence upon the energy of the sensitivity of PBI, GI and ABI. The SNR is inversely proportional to the square of the energy ($\mathrm{SNR} \propto 1/\mathrm{E}^2$) in PBI and GI, while it is inversely proportional to the energy ($\mathrm{SNR} \propto 1/\mathrm{E}$) in ABI, indicating better performance of ABI at high energies.

From a diagnostic point of view, Pagot *et al* (2005) showed that the image contrast of microcalcifications and infiltrating breast cancerous structures (which represent rapid phase variations) can be particularly high using PBI at large STDDs or in ABI with the analyzer crystal set at positions corresponding to the flanks of the RC. Masses with slow variations of the phase might be best rendered by ABI, which is sensitive to the gradient of the phase, rather than by PBI, which is sensitive to the Laplacian.

Crystal interferometry and ABI were experimentally compared in terms of density resolution by Yoneyama *et al* (2008). The analysis was performed on images of a CT phantom and different small biological samples. Depending on the specific experimental conditions (energy, number of images acquired), and for the used set-ups, the density resolution of crystal interferometry was found very similar or slightly higher than that of ABI in relatively homogeneous samples. Instead, ABI exceeded the other technique when density was measured in samples showing large density variations. This paper is an excellent demonstration not only of the variability of the results on the specific sample characteristics, but also of the high intrinsic difficulty of experimentally comparing results obtained with different techniques: the ABI set-up consisted of asymmetric (220) crystals, a not common set-up, showing a relatively large plateau on the top of the RC which reduces the angular sensitivity with respect to the typical triangular shape (figure 3).

6. X-ray sources for phase-contrast imaging

The application of PCI techniques in the imaging of tissues and organs has been limited by the restricted number of suitable x-ray sources. In fact, some of the methods require high transverse coherence (i.e. a small source) of the beam (GI, non-interferometric grating imaging and PBI), or longitudinal (high monochromaticity) coherence (ABI and crystal interferometry).

In practical terms, GI and PBI need a set-up where the sample 'sees' a small x-ray source, which is obtained when $L_{\mathrm{coh}} = \lambda R/s$ is large enough (is larger than the detail a to be imaged; here R is the distance to the source of size s). On the other hand, in both techniques, polychromatic radiation may be used without significant detriment of the achievable contrast.

In ABI and crystal interferometry the source size is not critical, but the perfect crystals reflect only narrow wavelength bands, which are small fractions of the total radiation spectrum of an x-ray tube; for a given source, this determines an increased imaging time with respect to techniques accepting polychromatic x-rays.

Obtaining a sufficient transversal or longitudinally coherent beam using conventional sources is possible, at the expenses of the exposure time that becomes too long for clinical imaging with any of the existing methods. Highly coherent beams are available at SR sources, where most of the PCI developments have been carried out till now. The access to SR sources is nevertheless limited and not applicable in the clinical practice if not for targeted clinical trials. For these reasons, in the recent years several solutions have been put forward to bridge the gap between conventional and large scale facilities.

The first commercial x-ray imaging system optimized for PBI mammography has been recently put on the market by Konica-Minolta (Regius Pureview®, http://www.konicaminolta.com/healthcare/technology/phasecontrast). It combines a small focal spot (0.1–0.3 mm), an image plate-like detector and a magnification system (source to image detector distance of 114 mm). The enhancement of the image contrast by PCI in breast tissue samples has been demonstrated, but there are no comparative clinical data yet (Honda and Ohara 2008, Williams *et al* 2008).

'Table-top' sources include a mini-synchrotron, where a circulating electron beam of high energy (order of 10 MeV) hits a wire or rod target, emitting a cone of Bremsstrahlung radiation in the forward direction (Hirai *et al* 2006). The spectrum of broad-band radiation can be tuned by the electron energy and the choice of the target material. The cone-shaped beam is well suited to GI and PBI (van Heekeren *et al* 2011). In a high-brilliance x-ray 'tube' the solid target is replaced by a jet of liquid metal (tin) or alloy (In-Ga) (Tuohimaa *et al* 2007, Larsson *et al* 2011), and a 50 kVp electron beam is focused on the jet. The spectral brilliance of the source is about 10 times higher than the brilliance of a micro-focus x-ray tube, and authors report that it may be possible to further increase the brilliance by one or two orders of magnitude.

Compact narrow-band SR sources are based on inverse Compton scattering, where a laser pulse is back-scattered as hard x-rays by a head-on collision with an electron bunch in a small-scale storage ring. Alternatively, the process can be described as SR emission when the electron bunch travels through the periodic electro-magnetic field of the laser pulse. The pulse interval is of the order of 10 ns, the radiation is collimated to a cone of a few mrad opening, and the energy bandwidth is of the order of 1%. Several light-sources are under construction or being commissioned, and their performance is expected to parallel the performance of bending magnet sources of large synchrotrons (Variola *et al* 2010, Lyncean Technologies, http://www.lynceantech.com). GI and PBI using an inverse Compton scattering source have been demonstrated (Bech *et al* 2009a, Yamada *et al* 2009), and the imaging performance of compact sources has been studied theoretically and by experiments (De Caro *et al* 2009, Oliva *et al* 2011). An alternative source of SR is the plasma of a gas-jet target, where electrons are trapped in an intense laser pulse and incur betatron oscillations emitting hard x-rays (Fourmaux *et al* 2011).

Conventional x-ray sources have been used in feasibility experiments, where imaging by various PCI methods has been demonstrated. X-ray tube sources have been used in several experiments with Talbot and Talbot–Lau interferometers (Bech *et al* 2009b, Zambelli *et al* 2010, Donath *et al* 2010), in the ABI set-up (Parham *et al* 2009, Faulconer *et al* 2009, Nesch *et al* 2009) and using the coded-aperture method (Olivo *et al* 2011). A prototype gantry system has been developed for CT imaging using a grating interferometer (Tapfer *et al* 2011).

7. Overview of the state of the art and technical challenges of the PCI techniques

All the PCI techniques presented in this review are used (or ready to be used) in preclinical research and, as it will be discussed in section 8, only PBI has yet reached the clinical implementation in pilot clinical trials at a SR source (Castelli *et al* 2011) or, as introduced in section 6, in commercial systems (Regius Pureview®, Konica-Minolta, Tokio, Japan). There are no publications discussing the technological steps to be performed towards the clinical implementation of the PCI techniques on a large scale. Theoretical studies and preliminary experiments (Diemoz *et al* 2012a, 2012b, Pagot *et al* 2005, Yoneyama *et al* 2008) indicate that under proper conditions all PCI techniques provide results that exceed those of absorption radiography and CT.

Each technique presents different technical and experimental requirements in terms of source size, beam monochromaticity, optical stability, necessity of multi-image acquisitions or limitations linked to the minimum dose to the sample, long acquisition times, etc (as already discussed). The existence of such constraints slows down the clinical implementation of the PCI methods, which is the final goal in most of the cases. Intense theoretical, engineering and software developments are presently on the way, as witnessed by the increased number of both technical related PCI papers and applications studies. Some advancements are technique-specific, but others, like that one presented by Zhao *et al* (2012) on an innovative method to reduce up to 75% the number of required projections in CT, can be applied to all imaging methods.

A detailed discussion of the limitations and on-going technical efforts for PCI would need a dedicated article, and is therefore outside the scope of the present review. For the sake of completeness and to stimulate further works on the subject, we wish anyway to highlight some aspects of the state of the art for the different techniques.

7.1. ABI

It has been implemented with x-ray energies up to 70 keV; the stability and temperature drifts of the crystal analyzer, typical of the first experimental studies, have been solved by using fast reacting feedback systems. The same analyzer crystal can cover a very wide energy range (20–100 keV) and experiments with samples as large as 15 cm have been performed. The technique has no very strong requirements in terms of source size. In its current implementation, for obtaining acquisition time compatible with *in vivo* imaging, an intense and monochromatic x-ray beam is needed as a source; this is presently available only at SR facilities. An important step towards the application with conventional sources has been recently presented by Connor *et al* (2012). With respect to image acquisition, it has been demonstrated that a single image, acquired at a suitable position of the RC, is highly meaningful for a full diagnosis (Sztrókay *et al* 2012).

7.2. Crystal interferometry

It requires a monolithic perfect silicon block from which three lamellar crystals are shaped (figure 4). This constitutes also one of the main limitations of the technique, because perfect silicon blocks can presently be produced only with a limited size. Therefore, the maximum sample thickness typically cannot exceed a few centimeters. In terms of beam and coherence requirements, those are similar to the ABI ones.

7.3. PBI

It is the simplest method to be implemented. No specific x-ray optics is needed. On the other hand, there are source size limitations to guarantee a good spatial coherence and thus edge signal enhancement. A sufficient sample to detector distance is also needed to let the signal propagate and diffract. The technique is weakly sensitive to the beam spectrum and works also with polychromatic radiation. The beam divergence and size are no limiting factors. A single image acquired at one STDD may be diagnostically significant. Depending on the sample, phase retrieval algorithms can be applied even to a single PBI image as described in Beltran *et al* (2010).

7.4. GI

Many efforts have been made in past years to boost this promising technique. Improvement in the grating construction technology has permitted to obtain field of view of about 5 cm, but the technology seems ready to cover larger fields. Gratings are tailored for a relatively narrow energy spectrum. To use the method at different energies, an apparatus with several sets of gratings is required and could be realized. Implementing the GI at energies above 60 keV by guaranteeing high visibility is instead not trivial. Depositing gold structures thicker than 100 microns on the absorption grating is still a technological challenge. For fast imaging, a sufficiently coherent source is needed to avoid the use of a third (source) grating, today used in conventional x-ray tube-based GI set-ups. Phase stepping is the most used image reconstruction method, giving best contrast and image quality. Nevertheless, important developments aiming at avoiding this time consuming procedure have been developed and tested (among them: Bennett *et al* (2010) and Diemoz *et al* (2011)). A new acquisition sequence has been recently proposed by Zanette *et al* (2012) that allows saving time and dose with respect to the standard phase stepping.

7.5. Grating non-interferometric methods

These are the most recently developed techniques. Requirements in beam monochromaticity and longitudinal coherence are among the weakest (Munro *et al* 2010c) in PCI. High energy imaging at energies close to 100 keV has been demonstrated (Olivo *et al* 2012) with tungsten made gratings. Also in this case specific gratings have to be built for a given energy range. No particular constraints concerning the grating size and pattern manufacturing presently exist, because their apertures and pitch are in the order of dozens of microns (Munro *et al* 2010a). This technique is in its early stage of development and still needs further development and demonstration that the obtainable image contrast can be as high as the one provided by other PCI methods.

8. Results

Many of the studies quoted in this section include results on phantoms and *in vivo* tissue samples. The examples are limited to imaging that may be projected to clinical applications. Breast, lung, joints, bones, vasculature and brain have been mostly imaged in *ex vivo* and *in vitro* samples and in few studies also in live animals. In some cases as-recorded CT images are shown, in other cases phase maps or differential phase maps are derived.

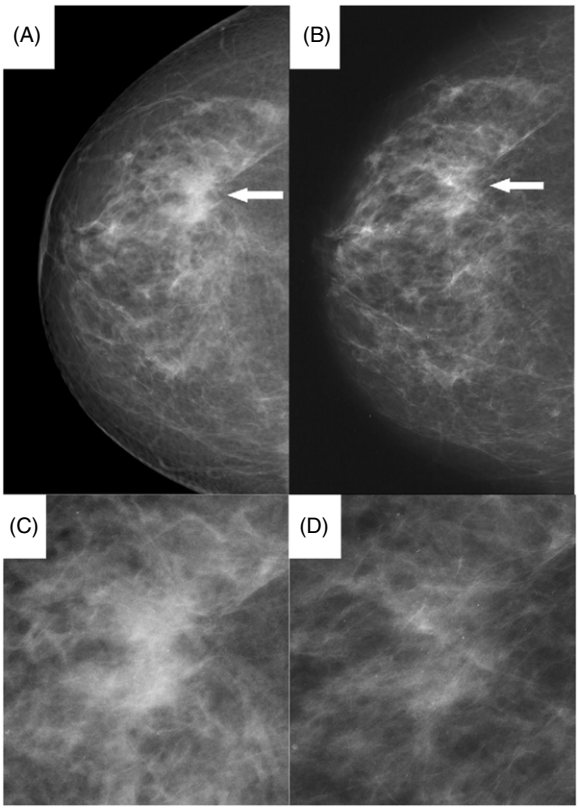

Figure 6. PBI images of right breast in 60-year-old woman with suspicious mass identified at DM. (a) Craniocaudal DM image and (b) corresponding digital zoom image show mass with architectural distortion (arrow) (BI-RADS category 4) in upper outer quadrant. (c) Findings on SR mammographic image and (d) corresponding digital zoom image do not confirm any suspicious breast masses (BI-RADS category 1). Imaging follow-up findings did not confirm any breast lesion. Reproduced, with permission, from Castelli *et al* 2011 *Radiology* **259** 684–94.

8.1. Breast

Phase-contrast imaging of the breast has been one of the first medical applications of x-ray PCI (Pisano *et al* 2000, Arfelli *et al* 2000). PCI mammography has been extensively reviewed recently (Keyriläinen *et al* 2010). So far, almost all studies have been based on PBI or ABI. PBI has been used in the planar (radiography) mode for comparisons with clinical absorption-contrast mammography. Pioneering experiments on excised breast tissue samples demonstrated the improved contrast (Arfelli *et al* 1998, 2000). These studies have led to the first clinical trials at the ELETTRA SR facility in Trieste, Italy (Castelli *et al* 2007, 2011). In this study 45 women, who had breast anomalies on basis of combined digital mammography (DM) and ultra-sonography, completed a protocol of SR mammography. The study also involved biopsy or follow-up for one year as the reference standards. The sensitivity of the SR mammography was 91% and the specificity as high as 94%. It was concluded that PBI-SR mammography is successful in the challenging case of clarifying diagnoses of questionable or suspicious breast anomalies identified by DM. A comparison of SR mammograms and DM is shown in figure 6. Studies comparing clinical radiographies of thick excised human samples

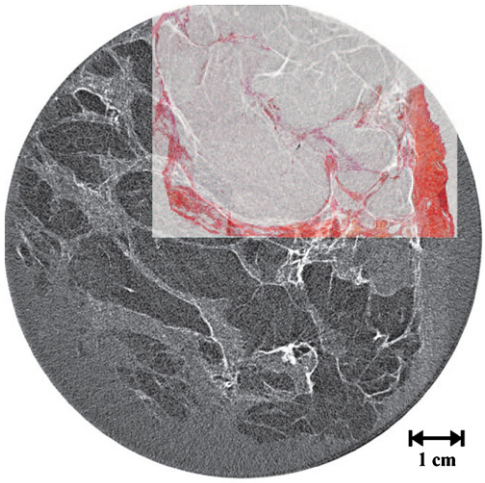

Figure 7. ABI-CT peak image of a 30 mm thick human breast tissue specimen with multifocal lobular carcinoma, obtained at 30 keV and with a mean glandular dose of 1.9 mGy. The ABI image is shown with an overlaid (50% transparent) optical image of the histopathologic whole-mount slide on the right upper quadrant of the specimen (Herovici stain; original magnification X1). The mature collagen appears red, and adipocytes appear white. Reproduced, with permission, from Keyriläinen *et al* 2008 *Radiology* **249** 321–7.

with ABI mammograms acquired using laboratory x-ray tubes have been reported (Parham *et al* 2009) showing that high contrast images can be obtained at very low doses.

There are several studies where the ABI method is used for imaging *in vitro* breast samples with the same goal of identifying mammographic signs in the images. Comparison of the same high resolution (∼20 lp mm^{-1}) CT slices with microscopy of histological images suggests that ABI-CT imaging may provide 'histo-pathology' of the breast both in partial (Keyriläinen *et al* 2008) and in full and large (150 mm diameter) organs (Sztrókay *et al* 2012). CT images in Keyriläinen *et al* (2008) were performed at radiation doses comparable with those used in a dual-view digital mammography (mean glandular dose ∼2 mGy). A microscopic image and ABI-CT image are overlaid in figure 7. The variant of ABI where non-deviated and refracted (+scattered) beams are separated by a thin Laue-type crystal has been used to image a small sample of breast tissue with ductal carcinoma *in situ* (Ando *et al* 2008).

The GI method has been used in a study of 'native' (freshly dissected) mastectomy samples, and the findings were compared with those from digital mammography, high-field MRI, ultra-sonography, and histo-pathology (Stampanoni *et al* 2011). A shield-tube x-ray source and Talbot–Lau interferometer were used, and with 8 phase steps, 5 cm × 5 cm planar images were acquired in 72 s. The mean glandular dose was 26 mSv, but this is expected to be substantially reduced by the use optimal beam filtering and a more efficient detector. The combination of absorption, refraction and scattering images contributed to better detection of mammographic signs, and the method seemed particularly well suited for examination of dense breast tissue.

In the above example dark-field image (scattering) revealed scar tissue and associated cancer invasion. It has been demonstrated that increased SAXS intensity arises from malignant changes in the structure of fibrous collagen and in granulation of smooth adipose tissue (Fernandez *et al* 2005, 2008), and these changes have been used as diagnostic indicators (Sidhu *et al* 2009). Following these findings, it could be envisaged that SAXS measurements

on biopsies would provide decisive information for cancer diagnosis; instead, the direct *in vivo* SAXS application is not feasible due to the high dose needed and the high mix up of the signal in a thick sample.

8.2. Musculoskeletal phase-contrast imaging

The lack of sufficient image quality and resolution in practically all medical imaging techniques (conventional radiology and CT, ultrasound, MRI) for an adequate visualization of articular cartilage has called for the development of new methods sensitive to stages preceding the point of irreversible damage of the cartilage tissue. X-ray PCI has been playing a valuable role in filling the gap in the capability of early and precise visualization of osteoarthritis (OA) and rheumatoid arthritis (RA) whose diagnosis implies the analysis of both soft tissue (i.e. cartilage) and (subchondral) bony details. Conventional imaging techniques are sensitive only at advance OA or RA stages when therapeutic strategies are less effective. Early studies demonstrated that the ABI technique could be a powerful tool in diagnostic orthopedics (Mollenhauer *et al* 2002, Muehleman *et al* 2004, Wagner *et al* 2005). Non-invasive detection of cartilage abnormalities, especially in the initial stages of degenerative joint disease (or early in its progression) was proven on very small samples and on excised human femoral heads. Both cartilage damages/fibrillations and trabecular bone meshwork could be simultaneously depicted at high spatial resolution. Other studies focused on healing of surgery procedures, i.e. metal implants in bone, whose assessment is very difficult with conventional imaging modalities. Destruction-free evaluation by ABI of the quality of the bone ingrowth into the implant surface was not only possible, but also much more sensitive than conventional radiography (Wagner *et al* 2006).

Application on excised full human joints using the CT acquisition mode demonstrated the ability of ABI to visualize internal architectural properties of the cartilage matrix in relatively large human cartilage samples (Coan *et al* 2008, Majumdar *et al* 2004). Fine cartilage anatomical features were visualized and a comparison with histology was also performed for OA and healthy tissues (Coan *et al* 2010a, Ismail *et al* 2010) (figure 8). AB images allowed differentiating osteoarthritic from normal samples in analogy to histopathological criteria. Micro-CT with SR and PBI has been instead used to visualize 3D osteon morphology with 1.4 μm spatial resolution (Cooper *et al* 2011).

A preliminary test of ABI on intact synovial joints, i.e. cadaveric human knee joints, has been carried out by Li and co-workers (Li *et al* 2009). Images demonstrate simultaneous soft tissue and bone contrast and clearly depict the articular cartilage, cruciate ligaments, loose connective tissue, menisci and chondrocalcinosis. ABI was also tested to assess the effectiveness of repair processes of bone tissue at a micro-level on rabbit model with osteonecrosis of the femoral head (Sun *et al* 2011).

Proof-of-principle studies of *in vivo* application of ABI were first performed by Coan *et al* (2010b): *in vivo* ABI radiographs and ABI-CT of guinea pigs knees were used to investigate the development of OA. Images give strong evidence of the ability of ABI in depicting both anatomic structures in complex systems (as living organisms) and clinical signs of osteoarthritis, with high contrast and high spatial resolution and at an acceptable radiation dose.

Recently, several groups have started exploring the possibility of applying the ABI technique on microfocus x-ray tubes. Images of an intact human knee showed the articular cartilage edge of the femoral condyle, even when superimposed by the tibia. In a thumb image, it was possible to visualize articular cartilage, tendons, and other soft tissues (Muehleman *et al* 2009). Lee *et al* (2010) reported the results of an *ex vivo* ABI-CT experiment aiming at

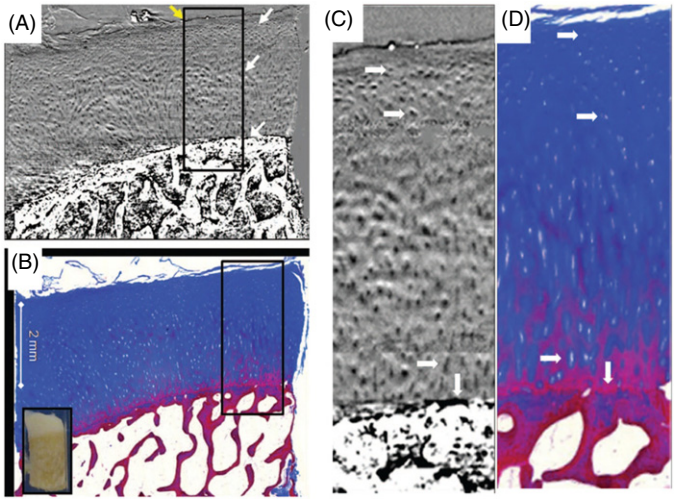

Figure 8. ABI-CT of a normal cartilage sample acquired at the 50% slope position of the analyzer crystal, at an x-ray energy of 26 keV, and using a detector pixel size of 8 μm2. Corresponding (to the extent that is possible practically) section from histologic preparation. (A) Coronal plane extracted from the reconstructed CT volume. (B) Histologic section (Azan staining); please note the original osteochondral cylinder (insert). (C and D) Magnified ROIs indicated by inserted rectangle from (A) and (B), respectively. Reprinted, with permission, from Coan *et al* 2010a *Invest. Radiol.* **45** 437–44.

visualizing the knee cartilages in a mouse model of collagen-induced arthritis. Agreement between ABI-CT images and histopathologic results was high.

Ex vivo GI images of an infant hand (Donath *et al* 2010) showed that tendons and ligaments appeared with strongly increased contrast-to-noise ratio with respect to comparative absorption-based images. Conventional x-ray tube-based GI images (Stutman *et al* 2011) of a cadaveric adult human finger showed that refraction-contrast was dominated by tendon embedded in muscle and that the cartilage layer was difficult to be observed. Nevertheless simulations on a joint model of the hand predict that a GI radiography could be feasible using optimized experimental parameters and set-up. First *in vivo* single-shot GI images (i.e. without phase-stepping) of rodent extremities, allowing a significant reduction of the imaging acquisition time, have recently opened the door to the preclinical application of the technique (Bennett *et al* 2010).

8.3. Lung

In conventional radiography, the lung is a weakly absorbing organ, and pathologies are seen as opaque masses. In the early ABI studies strong scattering contrast from the lung was observed (Zhong *et al* 2000). When the analyzer was tuned to the peak position, the apparent absorption in mouse lung was about four times larger than normal absorption, due to scatter rejection (extinction). The corresponding increase of scattering was observed when the analyzer was tuned to the tail of the RC. The specific surface area of the lung tissue is large and therefore giving rise to strong SAXS signal (equation 8). Scattering contrast would probably be used for research and diagnosis of diseases that lead to reduction of alveolar area of the lung (e.g. emphysema) as already shown in Kitchen *et al* (2011).

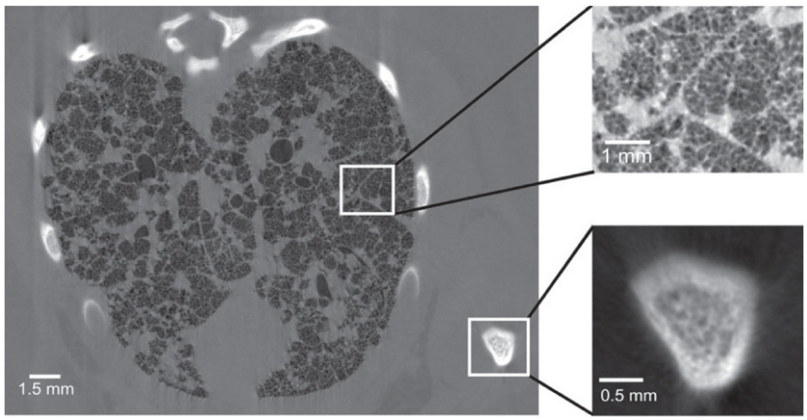

Figure 9. (a) Interface-specific phase retrieved-tomographic reconstruction from PBI data of a preterm rabbit pup thorax, focusing on the air/lung tissue interface. (b) Magnified section of (a) to aid visibility of the terminal airways. (c) Magnified section of (a) in which the bone/lung tissue interface appears blurred as a result of the chosen phase retrieval filter. Reprinted from Beltran *et al* 2011 *Phys. Med. Biol.* **56** 7353–69. Copyright 2011, with permission from the Institute of Physics and Engineering in Medicine.

Both ABI and PBI techniques have been used for studying lung structure and function (e.g. Parsons *et al* 2008, Beltran *et al* 2011) (figure 9). One research line is dynamical imaging of lung clearance at birth (Lewis *et al* 2005, Kitchen *et al* 2008, Hooper *et al* 2009). Rapid succession of PBI images of newborn rabbit pups locates airway liquid and allows visualization of lung aeration. This provides new and essential information about the transition to air-breathing at birth. Movement of fluid in airways, and reduction of the airway surface liquid, associated with cystic fibrosis have been imaged in a mice model *in vivo* (Siu *et al* 2008, Donnelley *et al* 2011). It has been observed that the projection image of lung has strong speckle pattern, and this was interpreted to arise from multiple refraction in alveoli, and to variable focusing of the x-ray beam (Kitchen *et al* 2004), like in an assembly of refractive lenses (Snigirev *et al* 1996). The speckle pattern is sensitive to the number of alveoli traversed by the beam, and this could probably be used for observing pathological changes in lung structure (Lewis *et al* 2005). Vessel stenosis and individual alveoli were imaged in excised rat and mice tissues (Zhang and Luo 2011). ABI has been used to detect atelectasis in an injured lung (Connor *et al* 2011), and imaging of the lung has been used as an example in development of a variant of the ABI method, where a Laue-type analyzer crystal splits the transmitted beam to direct and diffracted beams, which are recorded simultaneously at several rocking angles. Absorption, refraction and scattering images are retrieved by an iterative algorithm (Beltran *et al* 2011, Kitchen *et al* 2010, 2011).

8.4. Vasculature, circulation and soft tissue

Imaging of vasculature and circulation is traditionally based on absorption imaging, where the contrast is provided by a compound containing a heavy element (I, Ba, Gd). Contrast is enhanced by an order of magnitude when bi-chromatic SR and the K-edge subtraction technique is used (Suortti and Thomlinson 2003). 3D absorption CT with monochromatic SR and an area detector of micrometer resolution has revealed differences in microvascular networks of normal and tumoral brain tissue (Risser *et al* 2007).

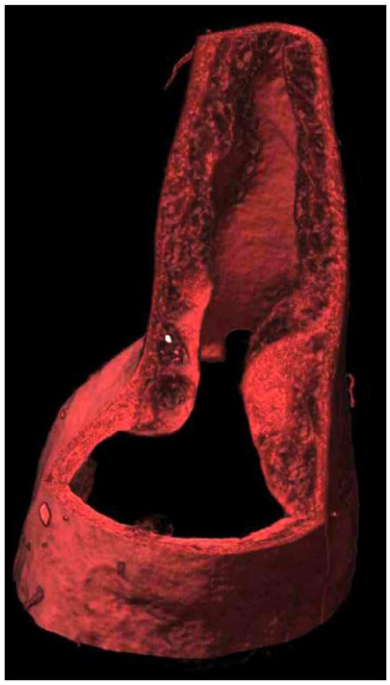

Figure 10. 3D phase rendering obtained with an x-ray crystal interferometer of the right common carotid artery of an ApoE-KO mouse that was fed a high-cholesterol diet. Scale bar: 1 mm. Reprinted, with permission, from Shinohara *et al* 2008 *Am. J. Physiol. Heart Circ. Physiol.* **294** H1094–100. Copyright 2008, American Physiological Society.

PCI with a crystal interferometer has been used for micro-CT of atherosclerotic plaque in mice that had been fed on high-cholesterol diet (Shinohara *et al* 2008, Takeda *et al* 2012a). The non-calcified plaque, which is not seen in high-resolution absorption CT, was clearly visible, and even different plaque components were identified on the basis of the phase maps (figure 10). The same method has been used for imaging glomeruli and tubular structures of kidney in hamsters, which had developed sclerosis (Wu *et al* 2009). Of potential high interest is the use of physiological saline for contrast enhancement in interferometric imaging of small-caliber hepatic vessels of rats *in vivo* (Takeda *et al* 2012b).

Gas-filled micro-bubbles are a standard contrast agent in ultra-sonography. Arfelli *et al* (2010) demonstrated that the same product can be used as PCI contrast agent: in fact, multiple-refraction or scattering from micrometer-size bubbles determine strong contrast in ABI. PBI was applied in an *ex vivo* experiment to visualize micro-vessels of mouse (Xi *et al* 2011), and to study *in vivo* angiogenesis in subcutaneous tumor (Tang *et al* 2011b). Both ABI and PBI techniques were used for imaging gastric cancer samples (Tang *et al* 2012). Gaseous contrast agents have been employed in other PCI applications: ambient air in the high resolution post-mortem visualization of the vascular tree in liver tissue CT imaging of mice (Laperle *et al* 2008) and CO_2 to image micro-vasculature in rat kidneys (Lundstrom *et al* 2012); micro-vasculature of the spinal cord has been successfully imaged without a contrast medium in a rat model by (Hu *et al* 2012) (figure 11).

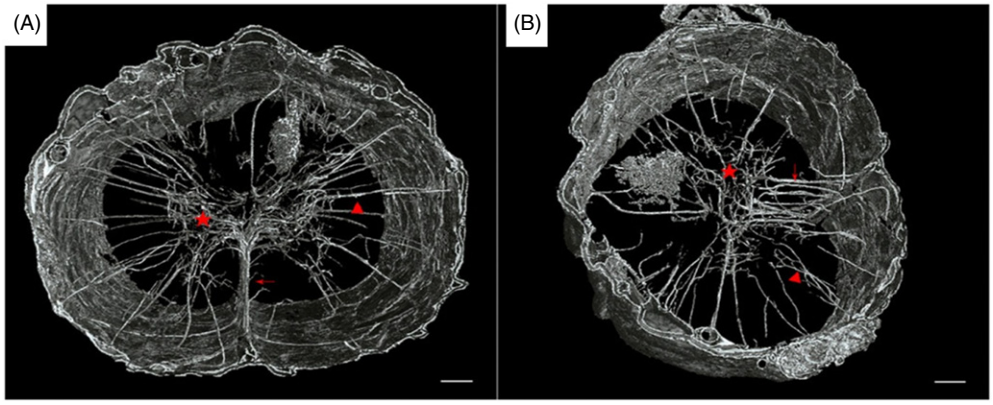

Figure 11. 3D angioarchitectural atlas in rat normal thoracic cord using the PBI technique. (A) The top view of the vasculature. (B) The oblique view of vasculature. Both (A) and (B) showed the main blood supply system in common, including the spinal anterior vessels, the spinal posterolateral vessels, the central sulcal vessels (arrow) and the rami perforating branches (triangle), and the micro-vessel networks were formed to feed the blood supply in gray matter (star). Bar = 100 μm. Reprinted from Hu *et al* 2012 *Phys. Med. Biol.* **57** N55–63. Copyright 2012, Institute of Physics and Engineering in Medicine.

8.5. Brain imaging

The advent of modern neuroimaging with CT and MR imaging allowed for a better diagnosis and characterization of brain abnormalities and diseases. Despite the deep insights offered by these imaging methods, their sensitivity and/or spatial resolution are insufficient to study at cell level the structures of this very complex tissue. The primary function of brain in the organism calls for sensitive and high resolution imaging modalities.

A few x-ray PCI experiments have been performed on brain tissues for verifying the potential of the method for neuroimaging applications. Most of the published studies have been conducted by using the GI technique in CT mode in both excised rat and human cerebella. GI images of a tumor bearing and healthy rat brain, respectively, clearly depicted the tumor tissue, the hippocampus and cerebellum regions (with white and gray matter) and the *substantia nigra* structure (Pfeiffer *et al* 2007, McDonald *et al* 2009, Rutishauser *et al* 2011) (figure 12). The application of the method to portions of human brain tissue allowed identifying besides the blood vessels, the *stratum moleculare*, the *stratum granulosum* and the white matter (Schulz *et al* 2010). Cochlear tissue samples have been imaged by GI and PBI to demonstrate the ability of visualizing soft tissue structures surrounded by bone (Richter *et al* 2009).

By using an innovative phase retrieval method applicable to a single distance PBI image, PBI-CT results showed demarcated tissue borders at the gray/white matter boundaries of a rat brain (Beltran *et al* 2011) and the visualization of subtle details in the brainstem, including the ventral cochlear nucleus, spinal tract of the trigeminal nerve and inferior cerebellar peduncle. This single image approach has clear benefits in terms of dose and acquisition time with respect to the multi-imaging modalities till here used in brain imaging by the other PCI techniques.

Another important application regarding the detection of core pathological features of Alzheimer's disease (AD). Current efforts in neuroimaging research aim at visualizing amyloid plaques, a hallmark feature of the AD, in living patients in order to evaluate the progression of the pathology, but also to facilitate its diagnosis. Because of their very small dimension and low radiographic contrast, amyloid plaques are not visible in conventional x-ray absorption-based

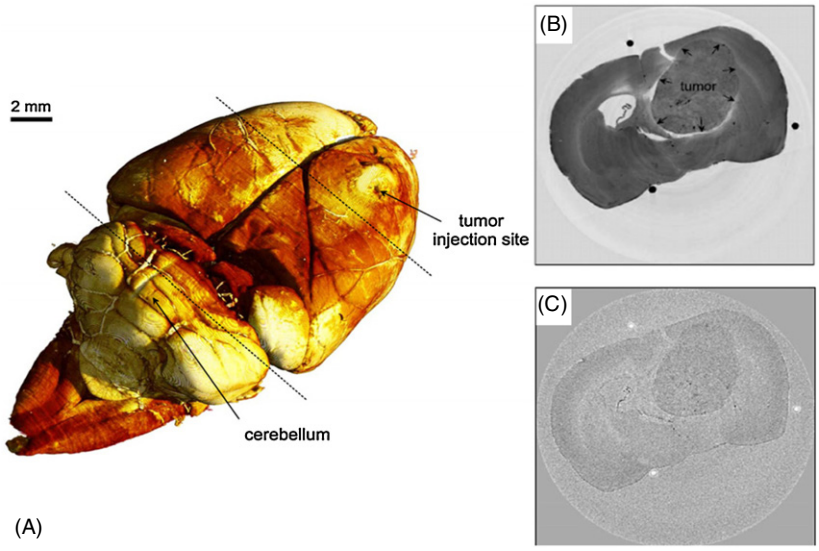

Figure 12. (A) Post mortem 3D GI image obtained on a rat brain bearing a 9L gliosarcoma. (B) Phase tomography slice through a region of the brain containing the tumor (arrows indicate the tumor's 'pushing front', the border between the tumor-invaded and healthy brain tissue). (C) Corresponding slice through the absorption-based reconstruction of the specimen. Reprinted from Pfeiffer *et al* 2007 *Phys. Med. Biol.* **52** 6923–30. Copyright 2007, Institute of Physics and Engineering in Medicine.

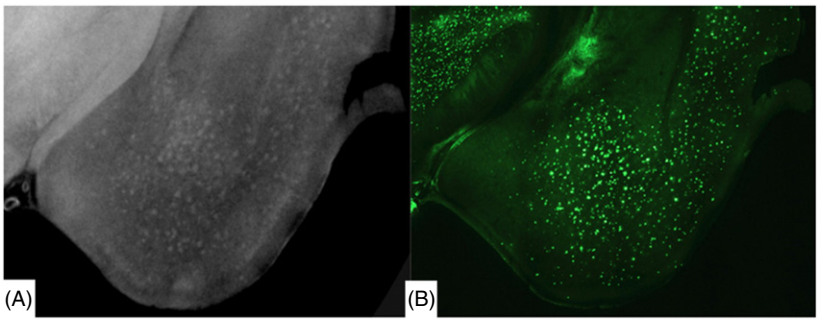

Figure 13. (A) Magnified unfiltered GI tomograms of a 5xFAD transgenic mouse brain at 13 months. The brain was extracted and fixed in paraformaldehyde 4% for one week at 4 °C and was scanned by DPC tomography with an isotropic voxel size of 7.4 μm. The 5xFAD brain was next sliced at 400 μm and stained with Thioflavin S to reveal amyloid deposits (B). Reprinted from Pinzer *et al* 2012 *Neuroimage* **61** 1336–46. Copyright 2012, Elsevier.

imaging. Proof of principle studies with both SR-based ABI (Connor *et al* 2009) and GI (Pinzer *et al* 2012) in micro-CT mode were performed on the brains of AD-model mice, demonstrating the ability of both techniques in visualizing the amyloid plaques as small nodules in the cortex and hippocampus of the brain (figure 13). These pioneering results already open the door to powerful studies aiming at quantifying the amyloid pathology in mouse models of AD and therefore might accelerate the evaluation of anti-amyloid compounds.

In addition, the PCI detection of fine brain features and cells without the application of any stain or contrast agent is an important result in the field of neuro-CT.

9. Discussions and conclusions

Phase-contrast imaging has become a paradigm in laboratory x-ray biomedical imaging; the pathway towards the clinical application has had a rapid acceleration over the past five years covered by this review. The literature has seen a rapid increase in the number of publications reporting the results of both biomedical applications and technical developments. *In vitro* and *in vivo* biomedical studies have focused on demonstrating and exploiting the high diagnostic significance of PCI images in a wide range of pathologies, including those of breast, joints, cartilage, lung and central nervous system. Results of the first clinical study in mammography performed at the ELETTRA SR source showed that PCI mammography (using the PBI technique) shows increased specificity and sensitivity with respect to conventional absorption-based x-ray radiography. Furthermore, the first commercial PCI-based clinical mammographic system (still using the PBI method) is now on the market; the results of its clinical use, not yet available, will represent a milestone for the further dissemination of PCI in the clinical practice.

The theoretical and technological developments reported in past years have stimulated the design of new PCI set-ups, have permitted to extend the range of applications towards higher x-ray energies (and therefore thicker samples), to diminish the imaging time (through new algorithms that need a reduced number of images to perform the phase retrieval), to increase the sensitivity of PCI. The impressive developments performed worldwide have made PCI the preclinical imaging reference in the visualization of several pathologies. Nevertheless, apart from the pilot projects already mentioned, there are still some technical factors limiting the immediate translation of PCI in the clinical practice: the main limitation concerns the time needed for an exam. For different reasons, all techniques can only use part of the beam delivered by a conventional x-ray source (a quasi monochromatic beam is required in ABI and in crystal interferometry or part of the beam is masked like in GI and non-interferometric methods). In this perspective, a promising solution is represented by the various compact x-ray source projects that have been put forward. These new sources aim at delivering quasi monochromatic x-ray beams with flux densities that are intermediate between those available at the large scale SR sources and at the clinical x-ray generators. These machines are therefore good candidates to boost the dissemination outside the SR sources of the PCI techniques applied *in vivo*.

Acknowledgments

We thank our collaborators and colleagues working in the field of biomedical applications of synchrotron radiation for making their latest results available. We also acknowledge several colleagues and friends from all around the world for their precious comments and suggestions during the redaction of this article. We are very grateful to the members of our research groups at the European Synchrotron Radiation Facility, the Ludwig Maximilians University, the MAP group and the University of Helsinki for their help in preparing this manuscript. We thank the authors, editors and publishers for their kind permission to reprint illustrations of previously published results. PC acknowledges support through the DFG Cluster of Excellence Munich—Centre for Advanced Photonics EXE158.

References

Anastasio M A, Shi D and Pan X 2009 Boundary-enhanced region-of-interest image reconstruction in propagation-based x-ray phase-contrast tomography *Appl. Phys. Lett.* **95** 244101

Anastasio M A *et al* 2010 Analysis of ideal observer signal detectability in phase-contrast imaging employing linear shift-invariant optical systems *J. Opt. Soc. Am.* **27** 2648–59

Ando M *et al* 2008 Refraction-based 2D, 2.5D and 3D medical imaging: stepping forward to a clinical trial *Eur. J. Radiol.* **68** S32–6

Appel A, Anastasio M A and Brey E M 2011 Potential for imaging engineered tissues with x-ray phase contrast *Tissue Eng. B: Rev.* **17** 321–30

Arfelli F, Rigon L and Menk R H 2010 Microbubbles as x-ray scattering contrast agents using analyzer-based imaging *Phys. Med. Biol.* **55** 1643–58

Arfelli F *et al* 1998 Low-dose phase contrast x-ray medical imaging *Phys. Med. Biol.* **43** 2845–52

Arfelli F *et al* 2000 Mammography with synchrotron radiation: phase-detection techniques *Radiology* **215** 286–93

Bech M *et al* 2009a Hard x-ray phase-contrast imaging with the compact light source based on inverse Compton x-rays *J. Synchrotron Radiat.* **16** 43–7

Bech M *et al* 2009b Soft-tissue phase-contrast tomography with an x-ray tube source *Phys. Med. Biol.* **54** 2747–53

Bech M *et al* 2010a Quantitative x-ray dark-field computed tomography *Phys.Med. Biol.* **55** 5529–39

Bech M *et al* 2010b Advanced contrast modalities for x-ray radiology: phase-contrast and dark-field imaging using a grating interferometer *Z. Med. Phys.* **20** 7–16

Beltran M A *et al* 2010 2D and 3D x-ray phase retrieval of multi-material objects using a single defocus distance *Opt. Express* **18** 6423–36

Beltran M A *et al* 2011 Interface-specific x-ray phase retrieval tomography of complex biological organs *Phys. Med. Biol.* **56** 7353–69

Bennett E E *et al* 2010 A grating-based single-shot x-ray phase contrast and diffraction method for *in vivo* imaging *Med. Phys.* **37** 6047–54

Bevins N *et al* 2012 Multicontrast x-ray computed tomography imaging using Talbot-Lau interferometry without phase stepping *Med. Phys.* **39** 424–8

Bonse U and Hart M 1965 An x-ray interferometer *Appl. Phys. Lett.* **6** 155–6

Bonse U and Hart M 1966 Small angle x-ray scattering by spherical particles of polystyrene and polyvinyltoluene *Z. Phys.* **189** 151–62

Bravin A 2003 Exploiting the x-ray refraction contrast with an analyzer: the state of the art *J. Phys. D: Appl. Phys.* **36** A24–9

Bravin A *et al* 2007 A numerical wave-optical approach for the simulation of analyzer-based x-ray imaging *Opt. Express* **15** 5641–8

Burvall A *et al* 2011 Phase retrieval in x-ray phase-contrast imaging suitable for tomography *Opt. Express* **19** 10359–76

Castelli E *et al* 2007 Clinical mammography at the SYRMEP beam line *Nucl. Instrum. Methods* A **572** 237–40

Castelli E *et al* 2011 Mammography with synchrotron radiation: first clinical experience with phase-detection technique *Radiology* **259** 684–94

Chapman D *et al* 1997 Diffraction enhanced x-ray imaging *Phys. Med. Biol.* **42** 2015–25

Chen G-H and Qi Z 2008 Image reconstruction for fan-beam differential phase contrast computed tomography *Phys. Med. Biol.* **53** 1015–25

Chen G-H *et al* 2010 Small-angle scattering computed tomography (SAS-CT) using a Talbot-Lau interferometer and a rotating anode x-ray tube: theory and experiments *Opt. Express* **18** 12960–70

Chen G-H *et al* 2011a Scaling law for noise variance and spatial resolution in differential phase contrast computed tomography *Med. Phys.* **38** 584–8

Chen R C *et al* 2011b Phase retrieval in quantitative x-ray microtomography with a single sample-to-detector distance *Opt. Lett.* **36** 1719–21

Chou C-Y and Anastasio M A 2009 Influence of imaging geometry on noise texture in quantitative in-line x-ray phase-contrast imaging *Opt. Express* **17** 14466–80

Chou C-Y and Anastasio M A 2010 Noise texture and signal detectability in propagation-based x-ray phase-contrast tomography *Med. Phys.* **37** 270–81

Chou C-Y and Huang P-Y 2011 Image reconstruction in phase-contrast tomography exploiting the second-order statistical properties of the projection data *Opt. Express* **19** 24396–410

Chou C Y *et al* 2007 An extended diffraction-enhanced imaging method for implementing multiple-image radiography *Phys. Med. Biol.* **52** 1923–45

Coan P *et al* 2010a Characterization of osteoarthritic and normal human patella cartilage by computed tomography x-ray phase-contrast imaging: a feasibility study *Invest. Radiol.* **45** 437–44

Coan P *et al* 2010b *In vivo* x-ray phase contrast analyzer-based imaging for longitudinal osteoarthritis studies in guinea pigs *Phys. Med. Biol.* **55** 7649–62

Coan P *et al* 2005 Phase-contrast x-ray imaging combining free space propagation and Bragg diffraction *J. Synchrotron Radiat.* **12** 241–5

Coan P *et al* 2008 Analyzer-based imaging technique in tomography of cartilage and metal implants: a study at the ESRF *Eur. J. Radiol.* **68S** S41–8

Cong W, Yang J and Wang G 2012 Differential phase-contrast interior tomography *Phys. Med. Biol.* **57** 2905–14

Connor D M *et al* 2009 Computed tomography of amyloid plaques in a mouse model of Alzheimer's disease using diffraction enhanced imaging *Neuroimage* **46** 908–14

Connor D M *et al* 2011 Diffraction enhanced imaging of a rat model of gastric acid aspiration pneumonitis *Acad. Radiol.* **18** 1515–21

Connor D M *et al* 2012 Preliminary performance measurements from a second generation diffraction enhanced imaging system *Proc. SPIE* **8313** 83134G

Cooper D M L *et al* 2011 Visualization of 3D osteon morphology by synchrotron radiation micro-CT *J. Anat.* **219** 481–9

David C *et al* 2002 Differential x-ray phase contrast imaging using a shearing interferometer *Appl. Phys. Lett.* **81** 3287–9

Davis T J *et al* 1995 X-ray image contrast from a simple phase object *Phys. Rev. Lett.* **74** 3173–6

De Caro L *et al* 2008 In-line phase-contrast imaging for strong absorbing objects *Phys. Med. Biol.* **53** 6619–37

De Caro L *et al* 2009 A theoretical study on phase-contrast mammography with Thomson-scattering x-ray sources *Med. Phys.* **36** 4644–53

De Caro L *et al* 2010 Combined mixed approach algorithm for in-line phase-contrast x-ray imaging *Med. Phys.* **37** 3817–27

De Caro L *et al* 2011 Deconvolution by finite-size-source effects of x-ray phase-contrast images *Med. Phys.* **38** 1951–61

Diemoz P C, Bravin A and Coan P 2012a Theoretical comparison of three x-ray phase-contrast imaging techniques: propagation-based imaging, analyzer-based imaging and grating interferometry *Opt. Express* **20** 2789–805

Diemoz P C, Bravin A, Langer M and Coan P 2012b Analytical and experimental determination of signal-to-noise ratio and figure of merit in three phase-contrast imaging techniques *Opt. Express* **20** 27670–90

Diemoz P C *et al* 2010a Comparison of analyzer-based imaging computed tomography extraction algorithms and application to bone-cartilage imaging *Phys. Med. Biol.* **55** 7663–79

Diemoz P C *et al* 2010b Absorption, refraction and scattering in analyzer-based imaging: comparison of different algorithms *Opt. Express* **18** 3494–509

Diemoz P C *et al* 2011 A simplified approach for computed tomography with an x-ray grating interferometer *Opt. Express* **19** 1691–8

Donath T *et al* 2010 Toward Clinical x-ray phase-contrast CT demonstration of enhanced soft-tissue contrast in human specimen *Invest. Radiol.* **45** 445–52

Donnelley M *et al* 2011 Synchrotron phase-contrast x-ray imaging reveals fluid dosing dynamics for gene transfer into mouse airways *Gene Ther.* **19** 8–14

Du Y *et al* 2011 Non-absorption grating approach for x-ray phase contrast imaging *Opt. Express* **19** 22669–74

Eastwood S A, Paganin D M and Liu A C Y 2011 Automated phase retrieval of a single-material object using a single out-of-focus image *Opt. Lett.* **36** 1878–80

Faulconer L *et al* 2009 Radiologist evaluation of an x-ray tube-based diffraction-enhanced imaging prototype using full-thickness breast specimens *Acad. Radiol.* **16** 1329–37

Feigin L A and Svergun D I 1987 *Structure Analysis by Small-Angle X-ray and Neutron Scattering* (London: Plenum)

Fernandez M *et al* 2005 Human breast cancer *in vitro*: matching histo-pathology with small-angle x-ray scattering and diffraction enhanced x-ray imaging *Phys. Med. Biol.* **50** 2991–3006

Fernandez M *et al* 2008 USAXS and SAXS from cancer-bearing breast tissue samples *Eur. J. Radiol.* **68** S89–S94

Förster E, Goetz K and Zaumseil P 1980 Double crystal diffractometry for the characterization of targets for laser fusion experiments *Krist. Tech.* **15** 937–45

Fouras A *et al* 2009 The past, present, and future of x-ray technology for *in vivo* imaging of function and form *J. Appl. Phys.* **105** 102009

Fourmaux S *et al* 2011 Single shot phase contrast imaging using laser-produced Betatron x-ray beams *Opt. Lett.* **36** 2426–8

Ge X *et al* 2011 Investigation of the partially coherent effects in a 2D Talbot interferometer *Anal. Bioanalytical Chem.* **401** 865–70

Glatter O and Kratky O 1982 *Small Angle X-ray Scattering* (London: Academic)

Gong S, Gao F and Zhou Z 2010 Improving visibility of x-ray phase-contrast imaging with Wiener filtering *J. X-Ray Sci. Technol.* **18** 279–92

Guinier A 1939 La diffraction des rayons x aux tres petits angles; application a l'etude de phenomenes ultramicroscopiques *Ann. Phys. (Paris)* **12** 161–237

Guo X J *et al* 2011 Improving image quality of x-ray in-line phase contrast imaging using an image restoration method *Opt. Express* **19** 23460–8

Gureyev T E *et al* 2004 Linear algorithms for phase retrieval in the Fresnel region *Opt. Commun.* **231** 53–70

Gureyev T E *et al* 2008 Some simple rules for contrast, signal-to-noise and resolution in in-line x-ray phase-contrast imaging *Opt. Express* **16** 3223–41

Gureyev T E *et al* 2009 Refracting Rontgen's rays: propagation-based x-ray phase contrast for biomedical imaging *J. Appl. Phys.* **105** 102005

Herzen J *et al* 2009 Quantitative phase-contrast tomography of a liquid phantom using a conventional x-ray tube source *Opt. Express* **17** 10010–8

Hirai T *et al* 2006 Refraction contrast 11 × -magnified x-ray imaging of large objects by MIRRORCLE-type table-top synchrotron *J. Synchrotron Radiat.* **13** 397–402

Hofmann R, Moosmann J and Baumbach T 2011 Criticality in single-distance phase retrieval *Opt. Express* **19** 25881–90

Honda C and Ohara H 2008 Advantages of magnification in digital phase-contrast mammography using a practical x-ray tube *Eur. J. Radiol.* **68** S69–72

Hooper S B *et al* 2009 Imaging lung aeration and lung liquid clearance at birth using phase contrast x-ray imaging *Clin. Exp. Pharmacol. Physiol.* **36** 117–25

Hu J-Z *et al* 2012 Visualization of microvasculature by x-ray in-line phase contrast imaging in rat spinal cord *Phys. Med. Biol.* **57** N55–63

Huang Z F *et al* 2007 Strategy of extraction methods and reconstruction algorithms in computed tomography of diffraction enhanced imaging *Phys. Med. Biol.* **52** 1–12

Ignatyev K *et al* 2011 Effects of signal diffusion on x-ray phase contrast images *Rev. Sci. Instrum.* **82** 073702

Irvine S C *et al* 2010 Assessment of the use of a diffuser in propagation-based x-ray phase contrast imaging *Opt. Express* **18** 13478–91

Ismail E C *et al* 2010 X-ray phase contrast imaging of the bone-cartilage interface *Appl. Radiat. Isot.* **68** 767–71

Itoh H *et al* 2011 Two-dimensional grating-based x-ray phase-contrast imaging using Fourier transform phase retrieval *Opt. Exp.* **19** 3339–46

James R W 1962 *The Optical Principles of the Diffraction of X-rays* (Bell and Sons: London)

Jiang M, Wyatt C L and Wang G 2008 X-ray phase-contrast imaging with three 2D gratings *Int. J. Biomed. Imaging* **2008** 827152

Kashyap Y S *et al* 2010 A variable-wavelength-based approach of phase retrieval for contrast transfer function based methods *J. Synchrotron Radiat.* **17** 799–803

Keyriläinen J, Fernández M and Suortti P 2002 Refraction contrast x-ray imaging *Nucl. Instrum. Methods* A **488** 419–27

Keyriläinen J *et al* 2008 Towards high-contrast breast CT at low radiation dose *Radiology* **249** 321–7

Keyriläinen J *et al* 2010 Phase-contrast x-ray imaging of breast *Acta Radiol.* **51** 866–84

Khelashvili G *et al* 2006 A physical model of multiple-image radiography *Phys. Med. Biol.* **51** 221–36

Kincaid R *et al* 2008 Development of ultrafast laser-based x-ray *in-vivo* phase-contrast micro-CT beamline for biomedical applications at advanced laser light source (ALLS) *Proc. Soc. Photo-Opt. Instrum. Eng.* **7078** 707818.1–.12

Kitchen M J *et al* 2004 On the origin of speckle in x-ray phase contrast images of lung tissue *Phys. Med. Biol.* **49** 4335–48

Kitchen M J *et al* 2007 Analyzer-based phase contrast image reconstruction using geometrical optics *Phys. Med. Biol.* **52** 4171–87

Kitchen M J *et al* 2008 Dynamic measures of regional lung air volume using phase contrast x-ray imaging *Phys. Med. Biol.* **53** 6065–77

Kitchen M J *et al* 2010 X-ray phase, absorption and scatter retrieval using two or more phase contrast images *Opt. Express* **18** 19994–20012

Kitchen M J *et al* 2011 Phase contrast image segmentation using a Laue analyzer crystal *Phys. Med. Biol.* **56** 515–34

Köhler T, Brendel B and Roessl E 2011 Iterative reconstruction for differential phase contrast imaging using spherically symmetric basis functions *Med. Phys.* **38** 4542–5

Kottler C *et al* 2007 A two-directional approach for grating based differential phase contrast imaging using hard x-rays *Opt. Exp.* **15** 1175–81

Krejci F, Jakubek J and Kroupa M 2010 Hard x-ray phase contrast imaging using single absorption grating and hybrid semiconductor pixel detector *Rev. Sci. Instrum.* **81** 113702

Langer M *et al* 2008 Quantitative comparison of direct phase retrieval algorithms in in-line phase tomography *Med. Phys.* **35** 4556–66

Laperle C M *et al* 2008 Low density contrast agents for x-ray phase contrast imaging: the use of ambient air for x-ray angiography of excised murine liver tissue *Phys. Med. Biol.* **53** 6911–23

Larsson D H *et al* 2011 A 24 keV liquid-metal-jet x-ray source for biomedical applications *Rev. Sci. Instrum.* **82** 123701

Lauzier P T *et al* 2012 Interior tomography in x-ray differential phase contrast CT imaging *Phys. Med. Biol.* **57** N117–30

Lee Y S *et al* 2010 Articular cartilage imaging by the use of phase-contrast tomography in a collagen-induced arthritis mouse model *Acad. Radiol.* **17** 244–50

Lewis R A 2004 Medical phase contrast x-ray imaging: current status and future prospects *Phys. Med. Biol.* **49** 3573–83

Lewis R A *et al* 2005 Dynamic imaging of the lungs using x-ray phase contrast *Phys. Med. Biol.* **50** 5031–40

Li J, Zhu P and Sun Y 2012 An approximate reconstruction method for helical cone-beam differential phase-contrast computed tomography images *Phys. Med. Biol.* **57** 2347–56

Li J *et al* 2009 Phase-sensitive x-ray imaging of synovial joints *Osteoarthritis Cartilage* **17** 1193–6

Liu Y *et al* 2011 X-ray spatial harmonic imaging of phase objects *Opt. Lett.* **36** 2209–11

Lundstrom U *et al* 2012 X-ray phase contrast for CO(2)microangiography *Phys. Med. Biol.* **57** 2603–17

Luu M B *et al* 2011 Quantitative phase imaging with polychromatic x-ray sources *Opt. Express* **19** 8127–34

Lynch S K *et al* 2011 Interpretation of dark-field contrast and particle-size selectivity in grating interferometers *Appl. Opt.* **50** 4310–9

Majumdar S *et al* 2004 Diffraction enhanced imaging of articular cartilage and comparison with micro computed tomography of the underlying bone structure *Eur. Radiol.* **14** 1440–8

Maksimenko A *et al* 2005 Computed tomographic reconstruction based on x-ray refraction contrast *Appl. Phys. Lett.* **86** 124105

McDonald S A *et al* 2009 Advanced phase-contrast imaging using a grating interferometer *J. Synchrotron Radiat.* **16** 562–72

Meng F, Liu H and Wu X 2009 Feasibility study of the iterative x-ray phase retrieval algorithm *Appl. Opt.* **48** 91–8

Modregger P *et al* 2011 Sensitivity of x-ray grating interferometry *Opt. Express* **19** 18324–38

Modregger P *et al* 2012 Imaging the ultrasmall-angle x-ray scattering distribution with grating interferometry *Phys. Rev. Lett.* **108** 048101

Mollenhauer J *et al* 2002 Diffraction-enhanced x-ray imaging of articular cartilage *Osteoarthritis Cartilage* **10** 163–71

Momose A 1995 Demonstration of phase-contrast x-ray computed-tomography using an x-ray interferometer *Nucl. Instrum. Methods* A **352** 622–8

Momose A 2003a Phase-sensitive imaging and phase tomography using x-ray interferometers *Opt. Express* **11** 2303–14

Momose A 2005 Recent advances in x-ray phase imaging *Japan J. Appl. Phys.* **44** 6355–67

Momose A *et al* 1996 Phase-contrast x-ray computed tomography for observing biological soft tissues *Nat. Med.* **2** 473–5

Momose A *et al* 2003b Demonstration of x-ray Talbot interferometry *Japan J. Appl. Phys.: 2 Lett.* **42** L866–8

Moosmann J, Hofmann R and Baumbach T 2011 Single-distance phase retrieval at large phase shifts *Opt. Exp.* **19** 12066–73

Moosmann J *et al* 2010 Nonlinear phase retrieval from single-distance radiograph *Opt. Express* **18** 25771–85

Morgan K S, Paganin D M and Siu K K W 2011a Quantitative single-exposure x-ray phase contrast imaging using a single attenuation grid *Opt. Express* **19** 19781–9

Morgan K S, Paganin D M and Siu K K W 2011b Quantitative x-ray phase-contrast imaging using a single grating of comparable pitch to sample feature size *Opt. Lett.* **36** 55–7

Muehleman C *et al* 2004 X-ray detection of structural orientation in human articular cartilage *Osteoarthritis Cartilage* **12** 97–105

Muehleman C *et al* 2009 Diffraction-enhanced imaging of musculoskeletal tissues using a conventional x-ray tube *Acad. Radiol.* **16** 918–23

Munro P R T, Ignatyev K, Speller R D and Olivo A 2010a Design of a novel phase contrast x-ray imaging system for mammography *Phys. Med. Biol.* **55** 4169–85

Munro P R T, Ignatyev K, Speller R D and Olivo A 2010b Limitations imposed by specimen phase gradients on the design of grating based x-ray phase contrast imaging systems *Appl. Opt.* **49** 3860–3

Munro P R T, Ignatyev K, Speller R D and Olivo A 2012 Phase and absorption retrieval using incoherent x-ray sources *Proc. Natl Acad. Sci. USA* **109** 13922–7

Munro P R T *et al* 2010c Source size and temporal coherence requirements of coded aperture type x-ray phase contrast imaging systems *Opt. Express* **18** 19681–92

Nesch I *et al* 2009 The design and application of an in-laboratory diffraction-enhanced x-ray imaging instrument *Rev. Sci. Instrum.* **80** 93702

Nesterets Y I 2008 On the origins of decoherence and extinction contrast in phase-contrast imaging *Opt. Commun.* **281** 533–42

Nesterets Y I and Wilkins S W 2008 Phase-contrast imaging using a scanning-double-grating configuration *Opt. Express* **16** 5849–67

Nesterets Y I *et al* 2006a Combined analyzer-based and propagation-based phase-contrast imaging of weak objects *Opt. Commun.* **259** 19–31

Nesterets Y I *et al* 2006b On qualitative and quantitative analysis in analyzer based imaging *Acta Crystallogr.* A **62** 296–308

Nugent K A 2007 X-ray noninterferometric phase imaging: a unified picture *J. Opt. Soc. Am.* A **24** 536–47

Olivo A, Diemoz P C and Bravin A 2012 Amplification of the phase contrast signal at very high x-ray energies *Opt. Lett.* **37** 915–7

Olivo A and Speller R 2007 A coded-aperture technique allowing x-ray phase contrast imaging with laboratory sources *Appl. Phys. Lett.* **91** 074106

Olivo A and Speller R D 2009 Deconvolution of x-ray phase contrast images as a way to retrieve phase information lost due to insufficient resolution *Phys. Med. Biol.* **54** N347–54

Olivo A *et al* 2001 An innovative digital imaging set-up allowing a low-dose approach to phase contrast applications in the medical field *Med. Phys.* **28** 1610–9

Olivo A *et al* 2011 Noninterferometric phase-contrast images obtained with incoherent x-ray sources *Appl. Opt.* **50** 1765–9

Oliva P *et al* 2011 Quantitative evaluation of single-shot inline phase contrast imaging using an inverse Compton x-ray source *Appl. Phys. Lett.* **97** 134104

Oltulu O *et al* 2003 Extraction of extinction, refraction and absorption properties in diffraction enhanced imaging *J. Phys. D: Appl. Phys.* **36** 2152–6

Paganin D *et al* 2002 Simultaneous phase and amplitude extraction from a single defocused image of a homogeneous object *J. Microsc. Oxford* **206** 33–40

Pagot E *et al* 2003 A method to extract quantitative information in analyzer-based x-ray phase contrast imaging *Appl. Phys. Lett.* **82** 3421–3

Pagot E *et al* 2005 Quantitative comparison between two-phase contrast techniques: diffraction enhanced imaging and phase propagation imaging *Phys Med. Biol.* **50** 709–24

Parham C *et al* 2009 Design and implementation of a compact low-dose diffraction enhanced medical imaging system *Acad. Radiol.* **16** 911–7

Parsons D W *et al* 2008 High-resolution visualization of airspace structures in intact mice via synchrotron phase-contrast x-ray imaging (PCXI) *J. Anat.* **213** 217–27

Pfeiffer F *et al* 2006 Phase retrieval and differential phase-contrast imaging with low-brilliance x-ray sources *Nat. Phys.* **2** 258–61

Pfeiffer F *et al* 2007 High-resolution brain tumor visualization using three-dimensional x-ray phase contrast tomography *Phys. Med. Biol.* **52** 6923–30

Pfeiffer F *et al* 2008 Hard-x-ray dark-field imaging using a grating interferometer *Nat. Mater.* **7** 134–7

Pinzer B R *et al* 2012 Imaging brain amyloid deposition using grating-based differential phase contrast tomography *Neuroimage* **61** 1336–46

Pisano E D *et al* 2000 Human breast cancer specimens: diffraction-enhanced imaging with histologic correlation-improved conspicuity of lesion detail compared with digital radiography *Radiology* **214** 895–901

Porod G 1951 Die Röntgenkleinwinkelstreuung von dichtgepackten kolloiden system I teil *Kolloidn. Zh.* **124** 83–114

Raupach R and Flohr T G 2011 Analytical evaluation of the signal and noise propagation in x-ray differential phase-contrast computed tomography *Phys. Med. Biol.* **56** 2219–44

Rayleigh L 1881 On copying diffraction-gratings, and on some phenomena connected therewith *Philos. Mag.* **11** 196–205

Ren Y *et al* 2011 Optimization of image recording distances for quantitative x-ray in-line phase contrast imaging *Opt. Express* **19** 4170–81

Revol V *et al* 2010 Noise analysis of grating-based x-ray differential phase contrast imaging *Rev. Sci. Instrum.* **81**

Richter C-P *et al* 2009 Imaging of cochlear tissue with a grating interferometer and hard x-rays *Micros. Res. Tech.* **72** 902–7

Rigon L, Arfelli F and Menk R-H 2007 Generalized diffraction enhanced imaging to retrieve absorption, refraction and scattering effects *J. Phys. D: Appl. Phys.* **40** 3077–89

Rigon L *et al* 2008 Generalized diffraction enhanced imaging: application to tomography *Eur. J. Radiol.* **68** S3–7

Risser L *et al* 2007 From homogeneous to fractal normal and tumorous microvascular networks in the brain *J. Cereb. Blood Flow Metab.* **27** 293–303

Rizzi J *et al* 2011 Quadriwave lateral shearing interferometry in an achromatic and continuously self-imaging regime for future x-ray phase imaging *Opt. Lett.* **36** 1398–400

Rutishauser S *et al* 2011 A tilted grating interferometer for full vector field differential x-ray phase contrast tomography *Opt. Express* **19** 24890–6

Ryan E A and Farquharson M J 2007 Breast tissue classification using x-ray scattering measurements and multivariate data analysis *Phys. Med. Biol.* **52** 6679–96

Sato G *et al* 2011 Two-dimensional gratings-based phase-contrast imaging using a conventional x-ray tube *Opt. Lett.* **36** 3551–3

Schmidt P W 1991 Small-angle scattering studies of disordered, porous and fractal systems *J. Appl. Crystallogr.* **24** 414–35

Schulz G *et al* 2010 High-resolution tomographic imaging of a human cerebellum: comparison of absorption and grating-based phase contrast *J. R. Soc. Interface* **7** 1665–76

Shinohara M *et al* 2008 Atherosclerotic plaque imaging using phase-contrast x-ray computed tomography *Am. J. Physiol. Heart Circ. Physiol.* **294** H1094–100

Sidhu S *et al* 2009 Mapping structural changes in breast tissue disease using x-ray scattering *Med. Phys.* **36** 3211–7

Siu K (eds) 2010 6th International Conference on Medical Applications of Synchrotron Radiation *Am. Inst. of Phys. (AIP) Conf. Proc.* p 1266

Siu K K W *et al* 2008 Phase contrast x-ray imaging for the non-invasive detection of airway surfaces and lumen characteristics in mouse models of airway disease *Eur. J. Radiol.* **68** S22–6

Snigirev A *et al* 1995 On the possibility of x-ray phase contrast microimaging by coherent high-energy synchrotron radiation *Rev. Sci. Instrum.* **66** 5486–92

Snigirev A *et al* 1996 A compound refractive lens for focusing high-energy x-rays *Nature* **384** 49–51

Stampanoni M *et al* 2011 The first analysis and clinical evaluation of native breast tissue using differential phase-contrast mammography *Invest. Radiol.* **46** 801–6

Stutman D *et al* 2011 Talbot phase-contrast x-ray imaging for the small joints of the hand *Phys. Med. Biol.* **56** 5697–720

Suhonen H *et al* 2005 Simulation of small-angle x-ray scattering from collagen fibrils and comparison with experimental patterns *Phys. Med. Biol.* **50** 5401–16

Suhonen H *et al* 2007 Refraction and scattering of x-rays in analyzer-based imaging *J. Synchrotron Radiat.* **14** 512–21

Sun W *et al* 2011 Experimental study on phase-contrast imaging with synchrotron hard x-ray for repairing osteonecrosis of the femoral head *Orthopedics* **34** E530–4

Suortti P and Thomlinson W 2003 Medical applications of synchrotron radiation *Phys. Med. Biol.* **48** R1–35

Sztrókay A *et al* 2012 High-resolution breast tomography at high energy: a feasibility study of phase contrast imaging on a whole breast *Phys. Med. Biol.* **57** 2931–42

Takeda M, Ina H and Kobayashi S 1982 Fourier-transform method of fringe-pattern analysis for computer-based topography and interferometry *J. Opt. Soc. Am.* **72** 156–60

Takeda M *et al* 2012a Beneficial effect of anti-platelet therapies on atherosclerotic lesion formation assessed by phase-contrast x-ray CT imaging *Int. J. Cardiovasc. Imaging* **28** 1181–91

Takeda T *et al* 2012b *In vivo* physiological saline-infused hepatic vessel imaging using a two-crystal-interferometer-based phase-contrast x-ray technique *J. Synchrotron Radiat.* **19** 252–6

Takeda Y *et al* 2008 Differential phase x-ray imaging microscopy with x-ray Talbot interferometer *Appl. Phys. Express* **1** 117002

Talbot H F 1836 Facts relating to optical science No. IV *Philos. Mag.* **9** 419–27

Tang L *et al* 2012 Synchrotron-radiation phase-contrast imaging of human stomach and gastric cancer: *in vitro* studies *J. Synchrotron Radiat.* **19** 319–22

Tang R *et al* 2011a Microbubble-based synchrotron radiation phase contrast imaging: basic study and angiography applications *Phys. Med. Biol.* **56** 3503–12

Tang X, Yang Y and Tang S 2011b Characterization of imaging performance in differential phase contrast CT compared with the conventional CT-Noise power spectrum NPS(k) *Med. Phys.* **38** 4386–95

Tapfer A *et al* 2011 Development of a prototype gantry system for preclinical x-ray phase-contrast computed tomography *Med. Phys.* **38** 5910–5

Tapfer A *et al* 2012 Experimental results from a preclinical x-ray phase-contrast CT scanner *Proc. Natl Acad. Sci. USA* **109** 15691–6

Teague M R 1983 Deterministic phase retrieval: a Green's function solution *J. Opt. Soc. Am.* **73** 1434–41

Thomlinson W, Chapman D L, Schültke E and Juurlink B H J (eds) 2008 Proceedings of the 5th medical application of synchrotron radiation 2007 *Eur. J. Radiol.* **68** S1–160

Thuering T *et al* 2011 Non-linear regularized phase retrieval for unidirectional x-ray differential phase contrast radiography *Opt. Express* **19** 25545–58

Tuohimaa T, Otendal M and Hertz H M 2007 Phase-contrast x-ray imaging with a liquid-metal-jet-anode microfocus source *Appl. Phys. Lett.* **91** 074104

van Heekeren J *et al* 2011 Characterization of an x-ray phase contrast imaging system based on the miniature synchrotron MIRRORCLE-6X *Med. Phys.* **38** 5136–45

Variola A, Loulergue A and Zomer F (eds) 2010 THOMX: conceptual design report *Technical Report* LAL RT 09/28; SOLEIL/SOU-RA-2678

Wagner A *et al* 2005 Options and limitations of joint cartilage imaging: DEI in comparison to MRI and sonography *Nucl. Instrum. Methods* A **548** 47–53

Wagner A *et al* 2006 Qualitative evaluation of titanium implant integration into bone by diffraction enhanced imaging *Phys. Med. Biol.* **51** 1313–24

Wang Z-T *et al* 2009 Quantitative grating-based x-ray dark-field computed tomography *Appl. Phys. Lett.* **95** 094105

Wang Z *et al* 2010a Analysis of polychromaticity effects in x-ray Talbot interferometer *Anal. Bioanalytical Chem.* **397** 2137–41

Wang Z *et al* 2010b Quantitative coherence analysis with an x-ray Talbot-Lau interferometer *Anal. Bioanalytical Chem.* **397** 2091–4

Weber T *et al* 2011 Noise in x-ray grating-based phase-contrast imaging *Med. Phys.* **38** 4133–40

Weitkamp T *et al* 2005 X-ray phase imaging with a grating interferometer *Opt. Express* **13** 6296–304

Weitkamp T *et al* 2008 X-ray phase radiography and tomography of soft tissue using grating interferometry *Eur. J. Radiol.* **68** S13–7

Wen H, Kemble C K and Bennett E E 2011 Theory of oblique and grazing incidence Talbot-Lau interferometers and demonstration in a compact source x-ray reflective interferometer *Opt. Express* **19** 25093–112

Wen H *et al* 2008 Spatial harmonic imaging of x-ray scattering initial results *IEEE Trans. Med. Imaging* **27** 997–1002

Wen H H *et al* 2010 Single-shot x-ray differential phase-contrast and diffraction imaging using two-dimensional transmission gratings *Opt. Lett.* **35** 1932–4

Wernick M N *et al* 2003 Multiple-image radiography *Phys. Med. Biol.* **48** 3875–95

Wilkins S W *et al* 1996 Phase-contrast imaging using polychromatic hard x-rays *Nature* **384** 335–8

Williams I M *et al* 2008 Towards the clinical application of x-ray phase contrast imaging *Eur. J. Radiol.* **68** S73–7

Wu J *et al* 2009 Imaging renal structures by x-ray phase-contrast microtomography *Kidney Int.* **75** 945–51

Wu X and Liu H 2007 Clarification of aspects in in-line phase-sensitive x-ray imaging *Med. Phys.* **34** 737–43

Wu X and Yan A 2009 Phase retrieval from one single phase contrast x-ray image *Opt. Express* **17** 11187–96

Wu X Z and Liu H 2005 X-ray cone-beam phase tomography formulas based on phase-attenuation duality *Opt. Express* **13** 6000–14

Xi Y *et al* 2011 Microbubbles as contrast agent for in-line x-ray phase-contrast imaging *Appl. Phys. Lett.* **99** 011101

Yamada K *et al* 2009 A trial for fine and low-dose imaging of biological specimens using quasi-monochromatic laser-Compton x-rays *Nucl. Instrum. Methods* A **608** S7–10

Yan A, Wu X and Liu H 2011 Robustness of phase retrieval methods in x-ray phase contrast imaging: a comparison *Med. Phys.* **38** 5073–80

Yoneyama A *et al* 2008 Quantitative comparison of imaging performance of x-ray interferometric imaging and diffraction enhanced imaging *Med. Phys.* **35** 4724–34

Zambelli J *et al* 2010 Radiation dose efficiency comparison between differential phase contrast CT and conventional absorption CT *Med. Phys.* **37** 2473–9

Zanette I *et al* 2011 Two-dimensional x-ray grating interferometer *Phys. Rev. Lett.* **105** 248102

Zanette I *et al* 2012 T. Trimodal low-dose x-ray tomography *Proc. Natl Acad. Sci. USA* **109** 10199–204

Zhang L and Luo S 2011 Micro soft tissues visualization based on x-ray phase-contrast imaging *Open Med. Inform. J.* **5 (Suppl. 1)** 19–25

Zhao Y *et al* 2012 High resolution, low dose phase contrast x-ray tomography for 3D diagnosis of human breast cancers *Proc. Natl Acad. Sci. USA* **109** 18290–4

Zhong Z *et al* 2000 Implementation of diffraction-enhanced imaging experiments: at the NSLS and APS *Nucl. Instrum. Methods* A **450** 556–67

Zhou S-A and Brahme A 2008 Development of phase-contrast x-ray imaging techniques and potential medical applications *Phys. Med.* **24** 129–48

Zhu P *et al* 2010 Low-dose, simple, and fast grating-based x-ray phase-contrast imaging *Proc. Natl Acad. Sci. USA* **107** 13576–81